Contrib Mineral Petrol (2012) 164:317–339
DOI 10.1007/s00410-012-0740-x

ORIGINAL PAPER

Amphibole stability in primitive arc magmas: effects of temperature, H_2O content, and oxygen fugacity

Michael J. Krawczynski · Timothy L. Grove · Harald Behrens

Received: 22 August 2011 / Accepted: 12 March 2012 / Published online: 7 April 2012

Abstract The water-saturated phase relations have been determined for a primitive magnesian andesite (57 wt% SiO_2, 9 wt% MgO) from the Mt. Shasta, CA region over the pressure range 200–800 MPa, temperature range of 915–1,070 °C, and oxygen fugacities varying from the nickel–nickel oxide (NNO) buffer to three log units above NNO (NNO+3). The phase diagram of a primitive basaltic andesite (52 wt% SiO_2, 10.5 wt% MgO) also from the Mt. Shasta region (Grove et al. in Contrib Miner Petrol 145:515–533; 2003) has been supplemented with additional experimental data at 500 MPa. Hydrous phase relations for these compositions allow a comparison of the dramatic effects of dissolved H_2O on the crystallization sequence. Liquidus mineral phase stability and appearance temperatures vary sensitively in response to variation in pressure and H_2O content, and this information is used to calibrate magmatic barometers-hygrometers for primitive arc magmas. H_2O-saturated experiments on both compositions reveal the strong dependence of amphibole stability on the partial pressure of H_2O. A narrow stability field is identified where olivine and amphibole are coexisting phases in the primitive andesite composition above 500 MPa and at least until 800 MPa, between 975–1,025 °C. With increasing H_2O pressure (P_{H_2O}), the temperature difference between the liquidus and amphibole appearance decreases, causing a change in chemical composition of the first amphibole to crystallize. An empirical calibration is proposed for an amphibole first appearance barometer-hygrometer that uses Mg# of the amphibole and f_{O_2}:

$$P_{H_2O}(\text{MPa}) = \left[\frac{\text{Mg\#}}{52.7} - 0.014 * \Delta\text{NNO}\right]^{15.12}$$

This barometer gives a minimum P_{H_2O} recorded by the first appearance of amphibole in primitive arc basaltic andesite and andesite. We apply this barometer to amphibole antecrysts erupted in mixed andesite and dacite lavas from the Mt. Shasta, CA stratocone. Both high H_2O pressures (500–900 MPa) and high pre-eruptive magmatic H_2O contents (10–14 wt% H_2O) are indicated for the primitive end members of magma mixing that are preserved in the Shasta lavas. We also use these new experimental data to explore and evaluate the empirical hornblende barometer of Larocque and Canil (2010).

Keywords Amphibole · Experimental petrology · Shasta · Water in magma · Subduction zone volcanism

Communicated by J. Hoefs.

M. J. Krawczynski (✉)
MIT/WHOI Joint Program, Cambridge, MA 02139, USA
e-mail: mjk181@case.edu

Present Address:
M. J. Krawczynski
Case Western Reserve University, Cleveland, OH 44106, USA

T. L. Grove
MIT, Cambridge, MA 02139, USA
e-mail: tlgrove@mit.edu

H. Behrens
Institut für Mineralogie, Leibniz Universität Hannover, Hannover, Germany
e-mail: h.behrens@mineralogie.uni-hannover.de

Introduction

This study examines the H_2O-saturated phase relations of two primitive arc magmas; a basaltic andesite and primitive magnesian andesite from the Mt. Shasta region, CA. Each

of these compositions represent examples of hydrous magmas in equilibrium with a mantle peridotite source at depth (Grove et al. 2003). The H_2O-saturated phase relations of the primitive magnesian andesite have been determined over a range of crustal pressures (0.1–800 MPa) and oxygen fugacities from NNO to NNO+3. Previous studies have shown that the phase assemblages and compositions in hydrous systems, especially liquidus temperatures and appearance of amphibole, are highly dependent on water content (Holloway and Burnham 1972; Anderson 1980; Medard and Grove, 2008), f_{O_2} (Helz 1973, 1976), and alkali content (Cawthorn and Ohara 1976). These studies agree that near liquidus crystallization of amphibole together with Ca-rich pyroxene (cpx) and olivine at 500–800 MPa can produce calc-alkaline liquids.

Previous experimental studies have focused on either tholeiitic basalts (Holloway and Burnham 1972; Helz 1973; Anderson 1980), more evolved andesitic and dacitic magmas that compositionally match evolved eruptive products (Allen and Boettcher 1983; Rutherford and Devine 1988; Grove et al. 1997; Prouteau and Scaillet 2003; Alonso-Perez et al. 2009), or primitive compositions with affinities to arcs but with experiments done over limited pressure ranges (Moore and Carmichael 1998; Blatter and Carmichael 1998; Pichavant and MacDonald 2007). These experimental studies along with studies of natural samples (Grove and Donnelly-Nolan 1986; Romick et al. 1992; Davidson et al. 2007) have shown that amphibole crystallizes from a wide variety of liquids at crustal pressures and can be an important fractionating phase in arc systems. Significant amphibole fractionation has been inferred to occur at arcs such as Panama (Hidalgo and Rooney 2010), Chile (Kratzmann et al. 2010), and globally (Davidson et al. 2007). Olivine-bearing, plagioclase-free amphibole cumulates have been identified in the Bonanza Jurassic arc in British Columbia (Larocque and Canil 2010), and the Adamello batholith (Tiepolo et al. 2011). High-Mg# amphiboles have also been found as xenocrysts/phenocrysts associated with olivine at Mt. Shasta and Pinatubo, and amphibole with very Mg-rich pyroxenes in the Mexican volcanic arc as well (Prouteau and Scaillet 2003; Grove et al. 2005; Blatter and Carmichael 1998). Because of this prevalence of evidence for near-liquidus amphibole fractionation, more experimental data at higher pressure, H_2O, and SiO_2 compositions are needed to determine the stability of amphibole. We extend the experimental data set to the primitive magnesian andesite and basaltic andesite compositional systems and explore the effect of P_{H_2O} on amphibole composition.

Amphibole has long been targeted for use in mineral geobarometry because of its dramatic chemical variability, its common occurrence in igneous rocks (particularly in plutonic environments), and the absence of other mineral assemblages in the rock that can be used to estimate crystallization pressure. Pioneering studies on natural amphibole barometry by Hammarstrom and Zen (1986), calibrated by correlation with estimates of metamorphic pressure in the contact aureole of the pluton, and experimentally calibrated barometers of Johnson and Rutherford (1989) and Schmidt (1992), have focused on evolved magmatic systems in the rhyolite to tonalite range. These barometers are all based on the aluminum content in the amphibole, and they are applicable only to rocks with mineral assemblages consisting of many phases, creating low thermodynamic variance. Such barometers are not relevant for amphiboles that crystallize from less evolved (andesitic to basaltic) magmas where as few as only two other minerals are present with melt. We have calibrated this compositional variation for two lavas, report our results as a new amphibole Mg# geobarometer-hygrometer, and apply the barometer-hygrometer to amphibole antecrysts in lavas from Mt. Shasta, CA.

Experiments

Starting materials

Experiments were conducted on two different bulk compositions. One is a primitive magnesian andesite, 85–41c, from the topographic saddle between the Whaleback and Deer Mountain, erupted as a cinder cone and associated lava flows, 18.5 km to the north-northeast of the Mt. Shasta summit (Baker et al. 1994). This is the high-silica (57 wt% SiO_2), high-MgO (9 wt% MgO), high Mg# (74) end member of a suite of primitive lavas from the Mt. Shasta region that have Mg#s >70, and contains Fo_{94} olivine antecrysts (Baker et al. 1994; Grove et al. 2003; Ruscitto et al. 2011). The second composition is a primitive basaltic andesite (Mg#=71), 85–44, erupted from Cinder Cone, 11 km to the northwest of the Mt. Shasta summit (Baker et al. 1994; Grove et al. 2003, 2005). This basaltic andesite is the low-silica (52 wt% SiO_2), high-MgO (10.5 wt% MgO) end member of the primitive lava suite that contains Fo_{90} equilibrium olivine. These lavas represent primitive inputs into the Mt. Shasta plumbing system and both are hydrous with pre-eruptive H_2O contents between 3 and 6 wt% H_2O (Anderson 1974; Grove et al. 2003; Ruscitto et al. 2011).

Whole rock samples of these two compositions were ground in an Al_2O_3 shatter box and then reground under ethanol by hand in an agate mortar to create experimental starting materials. The ground powders were melted at 1,700 °C in a Pt crucible in air for 2 h, then quenched in

the crucible by dropping it in water. The glass was extracted from the crucible and ground in an agate mortar. The ground glass was then remelted in air and quenched and crushed following the same procedures to ensure homogeneity. The compositions of the starting materials are reported in Table 1. Experiments were conducted on both the powdered rock and glass starting materials (Table 2).

Experimental procedures

Experiments at 200 and 800 MPa were carried out in the MIT experimental petrology laboratory in cold seal molybdenum-hafnium-carbide vessels and a 1/2" piston cylinder assembly, respectively. The 500 MPa experiments were carried out at the Institut fur Mineralogie, Hannover, Germany, in internally heated pressure vessels. For H_2O-saturated experiments, the presence of excess H_2O after the end of an experiment was used to assure the experiment remained H_2O saturated throughout the run.

For the 200 MPa and 915–1,070 °C experiments, the pressure medium was an argon-methane gas mixture in a ratio of 1,000:11. Methane breaks down to $C + 2H_2$ at the conditions of the experiment, and the partial pressure of H_2 outside the capsule slows water loss and sample oxidation by hydrogen diffusion through the gold capsule. Experiments were carried out in Au outer capsules and Au inner sample capsules (Table 2). A typical double capsule technique was used to control oxygen fugacity at the nickel–nickel oxide (NNO) or rhenium–rhenium oxide (RRO=NNO+2; Pownceby and O'Neill 1994) buffer conditions, with Pt inner capsules used to enclose the NNO buffer material and Au capsules for the RRO buffer material (Ulmer 1971). The outer capsule is welded at both ends, and inner capsules are welded at one end, but only crimped shut on the other to facilitate equilibration of the silicate charge with the buffer assemblage through the fluid phase. Experiments were quenched by inverting the pressure vessel and allowing the charge to drop to the water-cooled cold seal end of the pressure vessel.

In the 500 MPa and 945–1,025 °C experiments, pure argon gas or an argon-H_2 mixture was the pressure medium. All of these experiments were conducted in Au capsules, some at H_2O-saturated conditions and some with a mixed $H_2O - CO_2$ volatile component. Volatiles were added as free water and silver oxalate ($Ag_2C_2O_4$). Capsules for both the 200 and 500 MPa experiments were cooled with liquid N_2 and then welded shut and weighed pre- and post-welding to assure no water loss. Oxygen fugacity in the 500 MPa experiments was controlled at NNO by adding small amounts of hydrogen gas to the vessel, and the partial pressure of H_2 was measured directly using a hydrogen permeable Pt membrane. Experiments conducted at NNO+3 were done in pure Ar with no added H_2, utilizing an intrinsic f_{H_2} imposed by the H_2 permeable pressure vessel walls to buffer experiments at that level. The f_{O_2} of the oxidizing experiments was not specifically measured but the intrinsic internally heated pressure vessel f_{O_2} is known to vary between NNO+2.6 and NNO+3.5 (Schuessler et al. 2008) so we have assumed an average of NNO+3. A detailed experimental procedure for the Hannover internally heated pressure vessel laboratory is presented in Berndt et al. (2002). Capsules of 85-41c rock powder and powdered glass starting material were run simultaneously during some experiments. Phase assemblages for these runs were identical for both starting materials, and the compositions were analyzed and compared (Table 3). In this way, we were able to perform phase appearance reversals on 500 MPa experiments. Experiments were quenched using the rapid quench technique described in Berndt et al. (2002), and quench rates are about 150 °C/s (Benne and Behrens 2003).

Experiments at 800 MPa were carried out on the 1/2" piston cylinder apparatus at MIT (Boyd and England 1960). The capsule in this experimental design was an Au 'trash-can' (Ayers et al. 1992) in which an outer capsule is prepared with a small lip and is fitted with a lid that is cold welded by pressure. The lid seals when the piston load is applied to the capsule during pressurization before heating (Fig. 1). The outer Au trash-can capsule is surrounded by an unfired-pyrophyllite ring. During compression the pyrophyllite ring deforms with the Au capsule and helps avoid any shear stresses from developing. Two smaller capsules are placed inside the trash can. Both inner capsules were welded at one end and only crimped at the other. One is an Au capsule containing the sample, and the other is a Pt capsule containing the NNO solid state buffer. Starting material was the finely ground 85-41c rock powder. The experiments were carried out at H_2O-saturated conditions, and free water was added to both the inner and the outer Au capsule. The experiments were quenched by turning off the power. Experimental durations for all

Table 1 Starting materials for experiments

	SiO_2	TiO_2	Al_2O_3	FeO	MnO	MgO	CaO	Na_2O	K_2O	P_2O_5	Total	Mg#
85-41c	57.79	0.6	14.46	5.74	0.11	9.14	8.17	3.11	0.71	0.15	99.98	74
85-44	51.68	0.6	16.40	7.93	0.16	10.79	9.67	2.24	0.42	0.11	100	71

Table 2 Run conditions and products for hydrous experiments in Au capsules

Run #	Starting Material‡	H_2O-saturated†	T°C	MPa	Duration (hours)	f_{O_2}	Phases*	% ΔFe§
85-41c								
B1038	RP	Yes	1,050	800	7.4	NNO	olv(7) + opx(1) + cpx(9) + liq(81)	−16.7
B1133	RP	Yes	1,000	800	26	NNO	olv(<1) + opx(9) + cpx(11) + amph(14) + liq(66)	−1.8
B1160	RP	Yes	1,000	800	9.5	NNO	olv(4) + opx(7) + cpx(15) + amph(−2) + liq(75)	−6.5
41c-101	RP	Yes	1,070	203	25	NNO	olv + spnl	
41c-103a	G	Yes	945	489	101	NNO	opx + cpx + amph + liq	
41c-103b	RP	Yes	945	489	101	NNO	opx(9) + cpx(11) + amph(18) + liq(61)	−0.7
41c-106	G	7.7/6.0	975	490	66	NNO	opx(12) + cpx(14) + amph(3) + liq(70)	0.5
41c-107a	G	Yes	975	490	66	NNO	olv(14) + opx(−10) + cpx(16) + liq(79)	1.0
41c-107b	RP	Yes	975	490	66	NNO	olv(12) + opx(−7) + cpx(15) + spnl(<1) + liq(80)	−4.0
41c-108a	G	Yes	1,000	476	73	NNO	olv(8) + cpx(10) + liq(80)	−6.6
41c-108b	RP	Yes	1,000	476	73	NNO	olv(7) + cpx(10) + spnl(<1) + liq(82)	−6.7
41c-110	G	7.4/6.2	1,000	476	73	NNO	opx(12) + cpx(13) + liq(75)	−7.3
41c-111a	G	Yes	1,025	485	69	NNO	olv(7) + cpx(6) + spnl(<1) + liq(85)	−6.5
41c-111b	RP	Yes	1,025	485	69	NNO	olv(7) + cpx(6) + liq(86)	−12.3
41c-116b	RP	Yes	950	500	75	NNO+3	opx(4) + cpx(4) + amph(34) + spnl(<1) + liq(57)	−0.8
41c-117	G	7.7/2.4	975	500	52	NNO+3	opx(6) + cpx(8) + amph(19) + mag(<1) + liq(67)	−0.3
41c-118	G	6.4/6.4	975	500	52	NNO+3	opx(10) + cpx(12) + amph(13) + mag + liq(65)	−0.5
41c-119b	RP	Yes	975	500	52	NNO+3	opx(6) + cpx(8) + amph(14) + mag(1) + liq(72)	−0.3
41c-129	RP	Yes	915	201	47	NNO	opx(15) + cpx(10) + amph(22) + plag(23) + liq(30)	1.8
41c-141	RP	Yes	930	208	35	RRO	opx(13) + cpx(4) + amph(20) + plag(14) + liq(49)	2.8
85-44								
44-100	G	Yes	1,000	476	73	NNO	olv(12) + cpx(7) + liq(80)	−7.1
44-101	G	Yes	1,025	485	69	NNO	olv(11) + cpx(2) + liq(87)	−8.0
44–102	G	Yes	1,000	500	55	NNO+3	olv(3) + cpx(6) + amph(18) + mag(3) + liq(71)	0.2

Mineral abbreviations: olv–olivine, opx–orthopyroxene, cpx–high-Ca clinopyroxene, amph–amphibole, liq–glass (quenced liquid), spnl–Chromite, mag–magnetite, plag–plagioclase

‡ RP is a crushed rock powder starting material, and G is the glassed rock powder that was crushed and sieved

† Yes = experiment is H_2O saturated and wt% H_2O/wt%$Ag_2C_2O_4$ = experiments that are vapor saturated but mixtures of CO_2 and H_2O

* numbers in parentheses are the calculated modes of a particular phase calculated with a least squares linear regression mass balance

§ percent of relative Fe loss or gain from the starting material based on the difference between the starting material and calculated bulk composition of experiment using a linear regression mass balance

pressures were 7.4–26 h. Longer run times were not possible due to problems with Fe loss to the Pt buffer capsule or H_2O loss from the trash can (Table 2).

Analytical methods

Experimental run products were analyzed by electron microprobe on the JEOL 733 Superprobe at MIT. Beam conditions were 15 kV accelerating voltage and a 10 nA current. The CITZAF correction procedure of Armstrong (1995), using the atomic number correction from Duncomb and Reed, the absorption corrections with Heinrich's tabulation of mass-absorption coefficients, and the fluorescence corrections from Reed, was used to reduce the data and obtain quantitative analyses.

A materials balance calculation was used to estimate phase proportions and to determine whether FeO had been gained or lost from the experimental charge through reaction with the sample capsule. These results are reported in Table 2. Compositions of all of the phases are reported in Table 3. Errors reported are the $1-\sigma$ standard deviation of the arithmetic mean of replicate analyses on each phase. All glass analyses were done with a 10-micron-diameter beam to reduce Na-migration in the hydrous glass, and all mineral phases were analyzed with a focused 1–2 micron beam. Sodium analysis by microprobe is difficult with such hydrous glasses. Na-migration under the electron beam in these hydrous glasses results in lower Na_2O totals than expected. When comparing the Na_2O totals for the glass (Table 3) with that of the starting material (Table 1), and

Table 3 EMP analyses of experimental run products in oxide weight percents

Run	Phase	n	SiO_2[a]		TiO_2		Al_2O_3		Cr_2O_3		FeO		MnO		MgO		CaO		Na_2O		K_2O		P_2O_5		Total	Mg#
B1038	Glass	20	55.0	1.0	0.63	0.08	16.11	0.61	0.03	0.02	3.8	0.3	0.04	0.04	4.6	0.3	6.87	0.40	1.91	0.13	0.83	0.08	0.16	0.05	90.0	68.6
	Oliv	10	39.9	0.9	0.00	0.01	0.03	0.02	0.04	0.01	12.6	1.1	0.17	0.01	46.2	0.9	0.16	0.02							99.0	86.8
	cpx	18	53.5	1.0	0.26	0.08	1.84	0.51	0.55	0.20	4.6	0.9	0.12	0.04	18.5	0.6	20.38	0.80	0.25	0.05					100.1	87.7
	opx	9	56.3	0.6	0.13	0.03	1.11	0.27	0.29	0.15	9.4	1.1	0.19	0.03	30.8	1.1	1.72	0.37	0.00	0.00					100.0	85.3
B1133	Glass	19	57.5	0.5	0.43	0.06	17.84	0.16	0.01	0.01	4.3	0.1	0.10	0.02	2.9	0.2	5.96	0.23	2.89	0.30	0.32	0.09	0.13	0.04	92.4	54.8
	Oliv	13	39.0	0.5	0.01	0.01	0.02	0.01	0.03	0.02	16.7	0.7	0.21	0.03	44.6	0.9	0.13	0.04							100.6	82.7
	cpx	20	53.3	0.7	0.26	0.06	2.10	0.46	0.36	0.10	6.0	0.4	0.14	0.02	18.3	0.9	19.67	1.18	0.24	0.04					100.3	84.4
	opx	2	55.6	0.6	0.11	0.02	1.40	0.06	0.25	0.04	10.8	0.3	0.19	0.01	31.0	0.1	1.51	0.15	0.03	0.02					100.8	83.6
	Amph	12	45.1	0.6	1.31	0.20	11.57	0.37	0.54	0.34	7.2	0.5	0.11	0.02	17.8	0.3	11.44	0.34	2.29	0.06	0.19	0.02			97.5	81.5
B1160	Glass	19	54.1	0.9	0.64	0.07	17.42	0.26	0.04	0.02	4.0	0.2	0.10	0.02	3.5	0.4	6.61	0.37	2.12	0.46	0.60	0.06	0.17	0.03	89.2	60.9
	oliv	2	39.4	1.2	0.02	0.00	0.06	0.01	0.01	0.01	15.4	1.2	0.14	0.03	45.0	2.6	0.21	0.04							100.2	83.9
	cpx	11	53.7	0.7	0.29	0.05	2.22	0.31	0.15	0.14	5.6	0.7	0.15	0.04	17.9	1.1	20.20	1.27	0.25	0.06					100.5	85.1
	opx	7	55.9	0.7	0.14	0.04	1.76	0.59	0.08	0.05	10.1	0.5	0.20	0.04	30.2	0.8	1.71	0.59	0.04	0.03					100.1	84.2
	Amph	16	47.0	0.8	1.04	0.24	11.77	0.81	0.37	0.22	6.8	0.7	0.11	0.03	17.3	0.8	11.50	0.45	1.96	0.22	0.26	0.02			98.1	81.9
41c-101	Glass																									
	spnl	3	0.2	0.1	0.73	0.08	11.85	2.51	47.51	0.45	20.0	2.6	0.30	0.03	17.8	0.5	0.19	0.12							98.6	61.4
	Oliv	8	40.6	0.4	0.0	0.0	0.03	0.01	0.02	0.02	9.38	1.05	0.19	0.02	49.05	1.05	0.19	0.02							99.5	90.3
41c-103a	Glass																									
	cpx	12	54.6	0.5	0.26	0.05	1.83	0.40	0.24	0.07	6.3	0.5	0.14	0.03	17.6	0.5	19.60	0.83	0.19	0.05					100.7	83.3
	opx	11	56.0	0.7	0.13	0.03	1.44	0.37	0.15	0.04	11.4	0.2	0.24	0.03	28.5	0.6	1.72	0.28	0.01	0.01					99.6	81.6
	Amph	9	47.9	0.2	0.97	0.12	10.15	0.30	0.21	0.09	7.5	0.5	0.12	0.03	17.8	0.3	11.15	0.31	2.15	0.08	0.22	0.01			98.2	80.8
41c-103b	Glass	10	58.2	0.3	0.42	0.04	17.85	0.14	0.03	0.02	3.7	0.1	0.05	0.01	2.4	0.1	5.56	0.26	2.93	0.90	0.74	0.05	0.26	0.07	92.1	53.6
	cpx	12	52.7	0.4	0.33	0.08	2.76	0.31	0.16	0.08	6.5	0.7	0.16	0.03	16.8	0.4	20.45	0.56	0.30	0.07					100.3	82.1
	opx	12	55.1	0.7	0.15	0.05	1.86	0.85	0.06	0.03	12.6	0.9	0.20	0.02	29.3	0.6	1.66	0.46	0.03	0.02					101.0	80.6
	Amph	12	45.3	0.5	1.78	0.27	12.38	0.36	0.16	0.14	7.6	0.2	0.07	0.02	16.9	0.5	11.30	0.24	2.40	0.08	0.27	0.03			98.2	79.9
41c-106	Glass	10	55.9	0.7	0.54	0.05	17.43	0.18	0.01	0.01	4.2	0.2	0.09	0.02	3.3	0.2	6.33	0.20	3.59	0.17	0.89	0.02	0.19	0.42	92.5	58.6
	cpx	20	51.2	0.8	0.48	0.11	3.64	0.58	0.33	0.07	6.6	0.6	0.12	0.02	17.2	1.0	20.09	0.97	0.44	0.08					100.1	82.2
	opx	12	53.4	0.7	0.32	0.07	3.27	0.55	0.41	0.09	11.1	0.6	0.26	0.03	29.7	0.7	1.43	0.32	0.09	0.05					100.0	82.7
	Amph	16	44.5	0.6	1.33	0.22	10.72	0.59	0.20	0.07	9.2	0.3	0.10	0.03	16.8	0.4	11.42	0.76	2.10	0.13	0.33	0.08			96.7	76.4
41c-107a	glass	10	56.6	0.3	0.60	0.06	16.60	0.12	0.01	0.01	4.0	0.1	0.04	0.02	3.6	0.2	6.01	0.14	2.36	0.20	0.91	0.17	0.19	0.03	90.9	61.3
	Oliv	25	39.6	0.2	0.01	0.01	0.00	0.00	0.04	0.02	16.1	0.4	0.20	0.03	43.7	0.7	0.11	0.02							99.8	82.9
	cpx	12	53.8	0.5	0.32	0.07	2.47	0.52	0.56	0.13	5.5	0.5	0.13	0.02	17.4	0.6	20.04	0.86	0.26	0.05					100.5	84.9
	opx	9	56.2	0.5	0.10	0.04	2.06	0.54	0.23	0.08	8.7	0.5	0.16	0.04	30.4	0.5	1.71	0.13	0.03	0.02					99.6	86.2

Table 3 continued

Run	Phase	n	SiO_2[a]		TiO_2		Al_2O_3		Cr_2O_3		FeO		MnO		MgO		CaO		Na_2O		K_2O		P_2O_5		Total	Mg#
41c-107b	Glass	14	55.6	0.6	0.62	0.04	16.39	0.19	0.03	0.02	4.2	0.1	0.05	0.02	3.9	0.1	6.09	0.09	2.91	0.20	0.68	0.03	0.25	0.04	90.8	62.2
	spnl	6	0.2	0.1	0.70	0.09	14.44	1.39	46.3	1.4	27.5	1.1	0.31	0.02	9.6	0.4	0.22	0.06							99.3	38.5
	Oliv	9	40.1	0.3	0.00	0.01	0.01	0.02	0.03	0.02	13.2	1.3	0.17	0.03	46.4	1.2	0.15	0.02							100.1	86.3
	cpx	19	54.0	0.4	0.29	0.08	1.77	0.28	0.51	0.22	5.5	1.4	0.13	0.04	17.9	1.0	20.13	0.78	0.29	0.09					100.5	85.4
	opx	2	56.3	1.6	0.07	0.01	1.37	0.68	0.31	0.12	8.1	2.1	0.14	0.03	32.8	1.1	1.58	0.06	0.07	0.02					100.6	87.9
41c-108a	Glass	7	56.2	0.4	0.56	0.06	15.79	0.14	0.02	0.01	4.2	0.2	0.06	0.02	4.2	0.1	6.61	0.26	2.29	0.15	0.83	0.03	0.19	0.04	90.9	64.2
	Oliv	12	40.1	0.3	0.02	0.01	0.02	0.01	0.04	0.03	14.7	0.3	0.19	0.03	44.2	0.7	0.13	0.03							99.3	84.3
	cpx	16	54.2	0.4	0.27	0.04	2.11	0.41	0.55	0.14	4.9	0.4	0.13	0.04	18.0	0.6	20.25	0.77	0.23	0.06					100.6	86.7
41c-108b	Glass	14	54.9	0.5	0.63	0.04	15.69	0.13	0.04	0.02	4.4	0.1	0.05	0.02	4.5	0.1	6.45	0.29	2.79	0.14	0.67	0.04	0.23	0.03	90.4	65.0
	spnl	8	0.2	0.1	0.61	0.13	12.16	1.25	48.7	2.3	25.3	1.4	0.29	0.03	10.2	0.4	0.23	0.04							97.6	41.7
	Oliv	10	40.5	0.3	0.01	0.01	0.04	0.06	0.02	0.01	12.9	0.7	0.17	0.03	46.7	0.9	0.14	0.03							100.6	86.5
	cpx	14	53.7	0.5	0.24	0.07	1.82	0.56	0.67	0.25	4.6	0.9	0.11	0.03	17.7	0.3	21.40	0.80	0.27	0.07					100.5	87.3
41c-110	Glass	19	55.8	0.3	0.60	0.06	16.89	0.15	0.02	0.03	4.4	0.3	0.08	0.03	4.0	0.2	6.58	0.09	3.65	0.16	0.85	0.02	0.21	0.02	93.1	62.2
	cpx	20	52.6	0.7	0.43	0.07	3.14	0.45	0.36	0.05	5.9	0.5	0.15	0.03	17.3	0.8	19.91	1.03	0.37	0.08					100.1	84.0
	opx	10	55.6	0.7	0.18	0.03	2.14	0.64	0.25	0.06	9.1	0.7	0.20	0.01	30.6	0.6	1.81	0.55	0.07	0.07					99.9	85.7
41c-111a	Glass	14	55.8	0.2	0.59	0.08	15.07	0.08	0.00	0.01	4.5	0.1	0.09	0.02	5.2	0.1	7.03	0.09	2.27	0.19	0.81	0.04	0.16	0.03	91.5	67.2
	spnl	7	0.2	0.1	1.19	0.12	14.33	0.71	46.8	1.0	23.3	0.5	0.26	0.02	11.5	0.3	0.27	0.02							97.8	46.8
	Oliv	17	40.1	0.5	0.01	0.01	0.01	0.04	0.07	0.04	12.3	0.6	0.14	0.02	46.6	1.0	0.25	0.43							99.5	87.1
	cpx	10	54.4	0.4	0.15	0.03	1.42	0.33	0.72	0.19	4.1	0.4	0.11	0.03	18.6	0.7	20.58	1.20	0.26	0.05					100.4	88.9
41c-111b	Glass	15	55.5	0.4	0.62	0.11	15.05	0.07	0.03	0.04	4.2	0.2	0.08	0.02	5.3	0.1	6.94	0.19	2.44	0.15	0.78	0.05	0.18	0.02	91.1	68.9
	Oliv	9	39.9	0.3	0.03	0.01	0.04	0.01	0.04	0.02	12.5	0.3	0.18	0.03	47.2	0.6	0.18	0.03							100.0	87.1
	cpx	15	54.2	0.2	0.17	0.03	1.36	0.16	0.81	0.07	3.8	0.3	0.10	0.02	18.1	0.3	21.73	0.40	0.28	0.05					100.5	89.5
41c-116b	Glass	15	62.0	0.5	0.34	0.05	16.67	0.13	0.00	0.00	3.4	0.2	0.09	0.02	2.4	0.3	5.42	0.19	3.38	0.10	0.63	0.10	0.13	0.04	94.5	55.4
	spnl	6	0.1	0.0	0.53	0.13	10.47	1.70	44.8	1.2	31.9	2.7	0.40	0.03	8.5	0.4	0.23	0.04							96.9	32.1
	cpx	14	52.6	0.6	0.33	0.09	3.48	0.45	0.30	0.27	6.3	0.5	0.16	0.03	16.7	1.1	20.64	0.97	0.33	0.06					100.8	82.7
	opx	10	55.5	0.7	0.15	0.05	2.48	0.79	0.09	0.03	11.5	0.6	0.22	0.03	29.4	0.8	1.34	0.36	0.06	0.04					100.7	81.9
	Amph	16	45.4	0.3	1.37	0.28	12.01	0.38	0.09	0.04	8.4	0.4	0.11	0.02	16.7	0.4	11.21	0.24	2.04	0.08	0.22	0.02			97.5	78.1
41c-117	Glass	15	57.8	1.1	0.60	0.10	16.67	0.05	0.02	0.01	4.2	0.1	0.10	0.04	3.6	0.1	5.91	0.27	2.82	0.68	0.82	0.15	0.25	0.03	92.8	60.7
	cpx	7	51.2	0.6	0.42	0.07	4.03	0.29	0.24	0.04	6.2	0.3	0.18	0.03	16.3	0.3	20.86	0.29	0.40	0.03					99.8	82.4
	opx	8	55.4	0.8	0.18	0.03	2.64	0.84	0.16	0.05	8.5	0.4	0.24	0.03	31.7	0.6	1.60	0.19	0.04	0.02					100.5	87.0
	Amph	10	45.0	0.4	1.16	0.07	10.58	0.46	0.32	0.03	7.9	0.5	0.06	0.03	17.6	0.3	11.37	0.30	2.22	0.07	0.26	0.03			96.5	79.8
	mag	7	0.2	0.0	1.79	0.01	5.85	0.08	1.71	0.35	76.1	1.4	0.23	0.03	6.8	0.2	0.18	0.03							92.9	13.8
41c-118	Glass	15	59.0	0.3	0.47	0.09	17.22	0.14	0.02	0.02	3.9	0.2	0.09	0.01	3.2	0.1	5.92	0.18	3.40	0.14	0.93	0.02	0.18	0.02	94.3	59.0
	cpx	7	50.0	0.7	0.57	0.05	5.34	0.42	0.27	0.05	7.5	0.2	0.11	0.03	15.5	0.7	20.44	0.56	0.54	0.03					100.3	78.6
	opx	8	53.9	0.7	0.19	0.02	4.07	0.33	0.19	0.01	9.9	0.2	0.16	0.02	30.3	0.2	1.40	0.15	0.08	0.02					100.2	84.5
	Amph	11	44.0	0.4	1.44	0.05	11.96	0.24	0.26	0.06	8.7	0.3	0.13	0.06	16.7	0.2	11.43	0.27	2.30	0.06	0.27	0.02			97.2	77.3

Table 3 continued

Run	Phase	n	SiO_2[a]		TiO_2		Al_2O_3		Cr_2O_3		FeO		MnO		MgO		CaO		Na_2O		K_2O		P_2O_5		Total	Mg#
41c-119b	Glass	28	55.2	1.0	0.56	0.06	16.05	0.18	0.02	0.02	4.4	0.1	0.06	0.02	4.1	0.1	6.14	0.12	2.84	0.22	0.75	0.04	0.23	0.06	90.3	62.8
	cpx	15	52.9	0.7	0.26	0.06	2.15	0.48	0.44	0.29	4.7	0.6	0.11	0.01	17.6	0.8	20.96	0.81	0.31	0.06					99.4	87.0
	opx	10	56.8	0.5	0.10	0.02	1.45	0.31	0.24	0.13	7.4	0.5	0.17	0.03	32.8	0.8	1.23	0.24	0.04	0.01					100.2	88.8
	Amph	19	45.2	0.4	0.97	0.06	10.45	0.39	0.14	0.08	7.4	0.4	0.07	0.04	18.3	0.3	11.38	0.28	2.12	0.08	0.23	0.02			96.3	81.5
	mag	10	0.2	0.0	1.47	0.13	5.03	0.37	4.89	2.55	72.4	2.8	0.27	0.03	7.6	0.4	0.21	0.03							92.1	15.8
41c-129	Glass																									
	cpx	12	53.0	0.7	0.47	0.09	2.13	0.39	0.26	0.13	7.2	0.6	0.18	0.02	16.5	0.6	19.96	0.91	0.23	0.10					99.9	80.4
	opx	8	54.4	0.8	0.22	0.05	1.29	0.69	0.07	0.02	15.6	0.7	0.30	0.03	26.2	0.9	1.48	0.21	0.03	0.05					99.5	74.9
	plag	10	54.5	0.7			29.10	0.57			0.7	0.1			0.2	0.0	11.75	0.47	4.44	0.33	0.14	0.02			100.9	35.9
	Amph	13	44.7	1.1	2.70	0.38	9.94	0.71	0.22	0.15	9.5	0.3	0.11	0.03	15.7	0.6	11.26	0.63	2.17	0.13	0.28	0.03			96.6	74.7
41c-141	Glass	34	61.1	1.1	0.73	0.09	15.04	0.39	0.02	0.02	3.8	0.3	0.06	0.02	2.3	0.7	5.61	0.29	2.70	0.49	0.68	0.10	0.23	0.03	92.4	52.3
	cpx	13	52.7	0.5	0.55	0.09	2.30	0.34	0.21	0.06	6.7	0.3	0.17	0.03	16.7	0.5	20.59	0.74	0.27	0.04					100.1	81.7
	opx	10	55.3	0.5	0.18	0.04	0.92	0.33	0.07	0.03	13.4	0.6	0.28	0.03	28.9	0.7	1.47	0.31	0.03	0.02					100.5	79.3
	plag	17	50.2	0.7			31.66	0.52			0.5	0.1			0.1	0.0	14.48	0.37	3.09	0.21	0.06	0.01			100.2	26.0
	Amph	17	45.8	1.1	2.60	0.29	9.75	0.94	0.21	0.18	8.9	0.5	0.11	0.03	16.7	0.7	10.98	0.51	2.02	0.21	0.24	0.02			97.3	77.0
44-100	Glass	35	49.4	0.4	0.58	0.06	17.80	0.11	0.03	0.03	5.8	0.2	0.10	0.03	5.0	0.2	8.74	0.21	2.61	0.21	0.39	0.02	0.13	0.04	90.6	60.3
	Oliv	23	39.3	0.6	0.02	0.01	0.04	0.15	0.07	0.03	15.6	0.7	0.20	0.06	44.3	0.6	0.20	0.11							99.8	83.5
	cpx	20	52.2	1.0	0.34	0.09	3.39	0.79	0.50	0.24	5.4	0.7	0.14	0.02	16.8	0.7	21.07	1.06	0.29	0.06					100.1	84.6
44-101	Glass	15	49.3	0.4	0.61	0.08	16.96	0.12	0.02	0.01	6.1	0.2	0.14	0.03	5.9	0.1	9.32	0.14	2.28	0.14	0.43	0.02	0.17	0.02	91.2	63.6
	Oliv	9	39.8	0.3	0.03	0.01	0.03	0.01	0.05	0.02	13.9	0.5	0.23	0.02	46.2	0.7	0.21	0.02							100.4	85.6
	cpx	15	52.4	0.4	0.30	0.05	3.04	0.49	0.77	0.18	4.6	0.4	0.11	0.03	16.8	0.6	22.23	0.75	0.27	0.04					100.6	86.6
44–102	Glass	15	49.3	0.5	0.55	0.05	17.27	0.16	0.01	0.01	4.8	0.1	0.14	0.02	5.5	0.2	7.93	0.30	2.55	0.28	0.65	0.18	0.14	0.03	88.8	67.2
	Oliv	8	40.3	1.9	0.00	0.00	0.02	0.02	0.02	0.01	8.3	1.1	0.25	0.03	51.3	2.9	0.12	0.01							100.3	91.7
	cpx	15	50.6	2.1	0.34	0.14	4.16	1.46	0.10	0.04	5.6	1.0	0.15	0.03	16.3	1.2	22.14	0.43	0.30	0.05					99.8	83.7
	Amph	18	44.4	0.6	0.72	0.05	11.18	0.55	0.30	0.08	7.8	0.2	0.06	0.02	18.3	0.5	11.03	0.38	2.37	0.09	0.18	0.02			96.3	80.6
	mag	3	0.2	0.0	1.17	0.05	8.57	0.33	2.14	0.62	70.6	0.8	0.35	0.01	9.7	0.7	0.10	0.04							92.8	19.7

n number of probe analyses

[a] Columns directly following the oxide wt% are 1-σ errors from replicate analyses

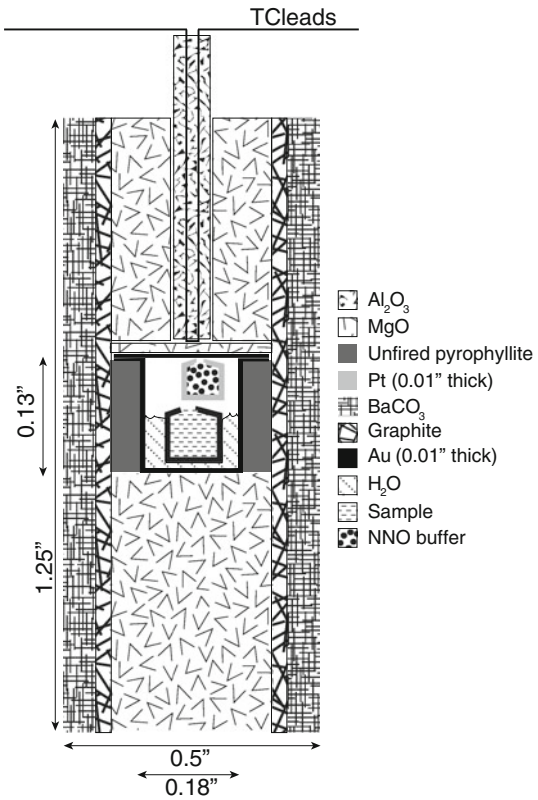

Fig. 1 Cross-section of the experimental assembly used in the 800 MPa 'trash-can' experiments. The outer Au capsule contains an inner capsule of sample material, a Pt buffer capsule, and enough free H_2O to ensure vapor saturation. There is a thin Au lid placed on the trash can and when the assembly is subjected to a 800 MPa piston load while cold, this junction is pressure welded shut

adjusting for crystal content of the experiments, there is a deficit of the Na_2O in glass analyses compared to the expected values.

Experimental results

Phase diagram and phase appearances

Run products for the experiments on the primitive magnesian andesite starting material are summarized in Table 2, and the phase assemblages and analyses are presented in Table 3. Typical examples experimental charges are shown in Fig. 2. At 0.1 MPa under anhydrous conditions, the phase appearance sequence has been previously determined by Grove et al. (2003). Spinel and olivine are liquidus phases at ~1,260 °C. Orthopyroxene (opx) appears at 1,210 °C, followed by plagioclase (plag) at 1,200 °C and then by clinopyroxene (cpx) at 1,160 °C. At 200 MPa and H_2O-saturated conditions, both olivine and spinel are still the liquidus phases; however, the liquidus drops by about 100 °C to 1,175 °C. Cpx joins the crystallizing phases at ~1,070 °C, and opx crystallizes at 1,030 °C. Olivine has reacted out by 1,000 °C and plagioclase crystallizes at approximately the same temperature. Amphibole does not crystallize until 920 °C, coexisting with less <50 % liquid.

At 500 MPa, the near-liquidus H_2O-saturated crystallization sequence is not as well constrained because of the low melting point of Au. Spinel, olivine, and cpx are still the high-temperature phases, and the appearance of cpx occurs at a temperature >1,025 °C. The appearance of opx is depressed by a further 40 °C to 990 °C, and plagioclase crystallization is depressed by >60 °C relative to the 200 MPa appearance because of the increase in dissolved H_2O content at these elevated pressures. Amphibole however appears 40 °C higher in the sequence compared to 200 MPa experiments (Fig. 3). The appearance of amphibole is related to the olivine-out reaction (Fig. 3) (Grove and Donnelly-Nolan 1986; Sisson and Grove 1993).

At 800 MPa orthopyroxene is present along with olivine and cpx in the highest temperature experiment at 1,050 °C, an increase of at least 60 °C from the 500 MPa experiments representing a change in sign of the slope of the opx-in curve with the minimum temperature in the curve at around 500 MPa. Also at 800 MPa amphibole appears between 1,000 and 1,050 °C, closer to the liquidus than amphibole appearance in lower-pressure experiments by at least 50 °C. Amphibole and olivine coexist in this experiment.

We were unable to determine water contents of the high-pressure experimental liquids. Due to the strong pressure dependence on the solubility of H_2O in silicate melts (Hamilton et al. 1964; Moore and Carmichael 1998; Mysen 2007), we expect that our highest pressure H_2O-saturated experimental liquids will contain >10 wt% H_2O. However, the liquids in experiments at 500 and 800 MPa quenched to vesiculated glasses, and microprobe analyses of the hydrous glasses show a deficit from 100 % totals of about 8–11 wt% (Table 3). We propose that this value represents the maximum quenchable H_2O content for this starting composition and experimental procedure, and the actual H_2O contents in the liquids are greater (see section "Evidence from amphibole for high magmatic H_2O in primary magmas from subduction zones" for estimates of H_2O contents).

Approach to equilibrium

Experimental durations were designed to be as long as possible for each experimental technique, to allow the experiments to reach equilibrium. Practical limitations were the exhaustion of the buffer assemblage or loss of H_2O from the capsule by diffusion of H_2 through the outer capsule wall. For the 200 and 500 MPa experiments,

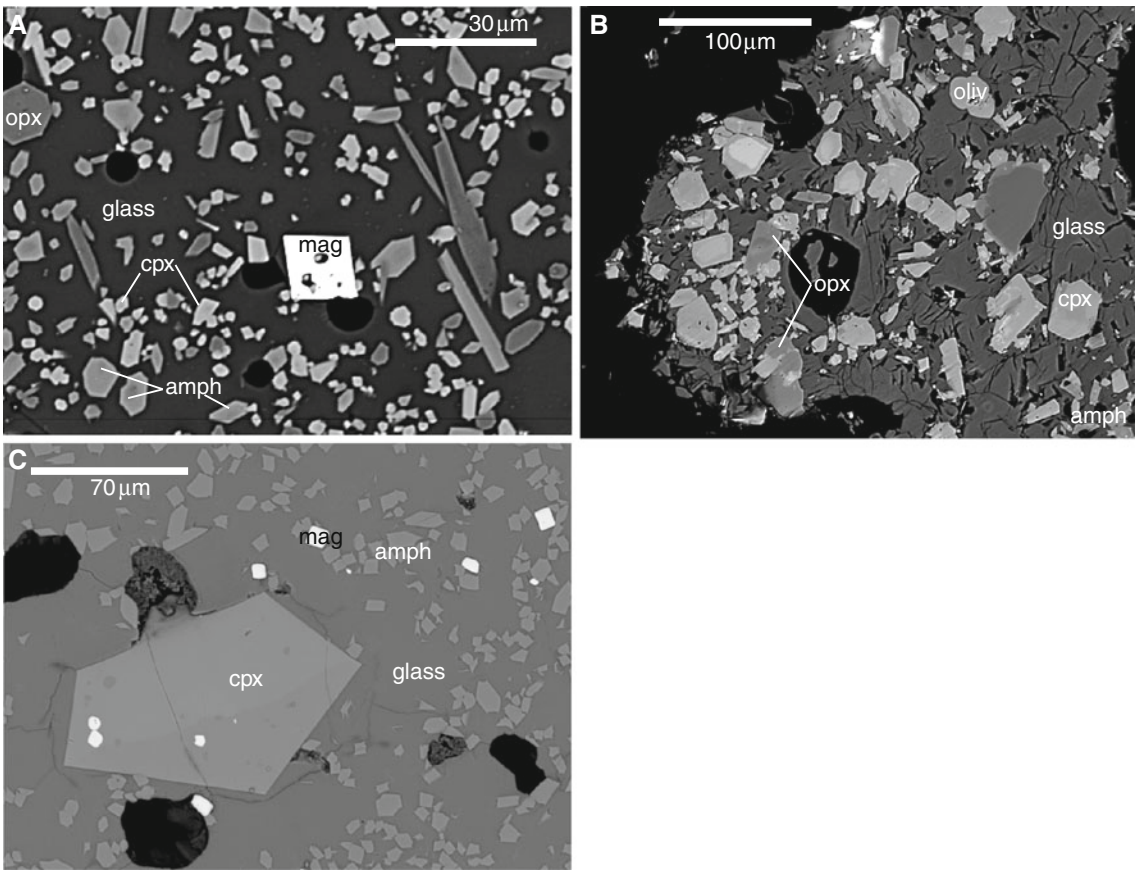

Fig. 2 Backscattered electron images of experimental run products. **a** Experiment 41c-117, 975 °C, 500 MPa, NNO+3, and mixed volatile. Crystals are opx, cpx, amphibole, and magnetite set in a matrix of quenched and slightly vesiculated glass. **b** Experiment B1160, 1,000 °C, 800 MPa, NNO, H_2O saturated. Visible crystals are olivine, amphibole, cpx, and over growths of equilibrium opx on unreacted pyroxene cores from the starting material, set in a matrix of vesiculated glass. **c** Experiment 44–102, 1,000 °C, 500 MPa, NNO+3, H_2O saturated. *Small gray crystals* are amphibole, *bright white crystals* are magnetite, and the *large crystal* is a sector zoned cpx, set in a matrix of vesiculated glass

typical experimental durations were 24–72 h and at 800 MPa experiments were run for between 7–26 h. The experimental durations for hydrous experiments were found to be sufficient to reach equilibrium crystallization conditions by Sisson and Grove (1993). Crystal morphology and the homogeneous nature of the run products are a good indication that equilibrium was reached.

A multiple linear regression mass balance calculation was used to obtain the phase proportions in each experiment and check for loss of Fe due to interaction with the capsule material (Table 2). Results of this mass balance show that Fe-loss is typically <7 wt%, but not negligible, especially in higher pressure runs. In the 500 MPa experiments, the large volume of the internally heated pressure vessel allowed us to run multiple experiments simultaneously using both a glass starting material and a powdered rock starting material. The results of these experiments are reported in Tables 2 and 3, and the compositions of phases in these runs are very similar.

Effects of P, H_2O, f_{O_2} on mineral chemistry for primitive magnesian andesite

Olivine

At 200 MPa, there is a 90 °C gap between the olivine and amphibole stability fields, with the most Fe-rich, low temperature olivine being $Fo_{81.7}$. At 500 MPa, forsterite contents in the experimental olivines range from 87.1 mol% at 1,025 °C to 84.6 mol% at 975 °C. Based on the experimental brackets, there is a maximum gap of 30 °C between the amph and olivine stability fields at 500 MPa under H_2O-saturated conditions, but amphibole and olivine may coexist over a very small temperature range. At 800 MPa, the olivines range from $Fo_{86.8}$ at 1,050 °C to $Fo_{83.3}$ at 1,000 °C. At 800 MPa and 1,000 °C, olivine coexists with amphibole that has a Mg# of 81.7. The Fo content and amph Mg# are calculated as the average of a pair of experiments that were run at the same

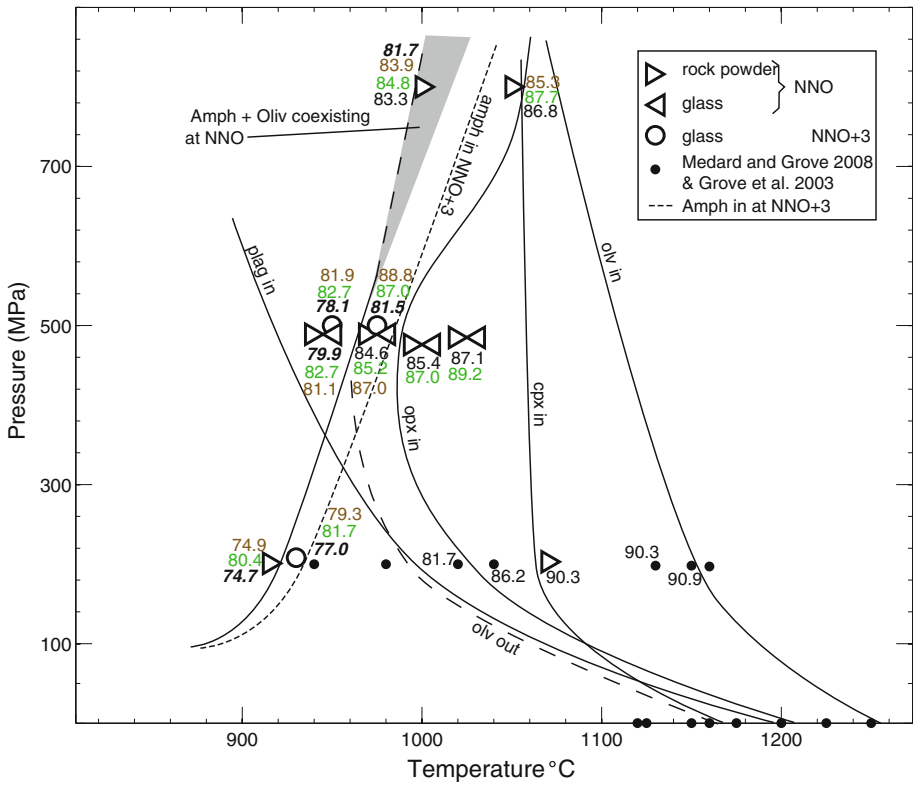

Fig. 3 *Phase diagram* showing all water-saturated experiments on the primitive magnesian andesite composition. Phase appearance *lines* for experiments at NNO are thin *black lines*, olivine disappearance is demarcated by a *long-dashed line*, and amphibole stability in NNO+3 experiments are the *short-dashed lines*. Mg# of Fe-Mg phases are also show in numbers next to each experiments, *black* for olivine, *green* for cpx, brown for opx, and *bold italic* for amphibole Mg#s. Amphibole is stabilized to higher T at oxidizing conditions. Above 500 MPa, there is a narrow zone of coexistence between olivine and amphibole and is denoted with a *gray field*

conditions. Coexistence of olivine and amphibole is restricted to a narrow range of temperature, above 500 MPa pressure, and at high H_2O contents (Fig. 3).

Clinopyroxene

The temperature of the first appearance of cpx in the H_2O-saturated crystallization sequence is relatively constant from 200 to 800 MPa. At 500 MPa, and NNO f_{O_2}, the cpx ranges from Mg# 89.2 coexisting with $Fo_{87.1}$ olivine at 1,025 °C to Mg# 82.7 coexisting with Mg# 79.9 amphibole at 945 °C. The NNO+3 experiments at 950 and 975 °C have cpx of 82.7 and 87.0 Mg#, respectively. There appears to be no systematic variation in cpx aluminum content over the pressure and temperature range investigated.

Orthopyroxene

At 200 MPa, the 85-41c experiments have orthopyroxene coexisting with cpx, amphibole, and plagioclase. The opx Mg# is 74.9 in our 915 °C experiment at NNO, and 79.3 at 930 °C and RRO. There is a minimum temperature for the opx-in curve that occurs at around 500 MPa. The first opx to crystallize at 500 MPa is Mg# 87.0 at NNO, and 88.8 at NNO+3, at 975 °C. At 800 MPa, opx is present at 1,000 °C and has a lower Mg# at 85.3.

In the H_2O-undersaturated experiments at 500 MPa and 1,000 °C, opx+cpx are the stable Fe-Mg silicates, replacing the assemblage of olivine+cpx in the H_2O-saturated experiments. The effect of water is to stabilize opx closer to the liquidus at these elevated pressures. The opx in the H_2O-undersaturated experiment has an Mg# of 85.7, lower than the first opx to crystallize in the H_2O-saturated experiments.

Plagioclase

Plagioclase is only stable in 200 MPa experiments below 1,025 °C. At 915 °C, NNO the plagioclase is $An_{58.9}$ and at 930 °C and NNO+3 the plag is $An_{71.9}$. For comparison, 1-atm pressure experiments on the same bulk composition show the first plagioclase to crystallize is at 1,200 °C and is $An_{62.1}$ (Grove et al. 2003).

Oxides

Magnetite is present in all experiments conducted at 500 MPa and NNO+3 including both the 85-41c and 85-44 starting materials. This phase is not stable in any of the experiments at NNO. When the magnetites were large enough to get accurate electron microprobe data, mass balance calculations show that the magnetite has a phase abundance by mass of 3 % or less. For experiments

conducted on the 85-41c starting material, the composition of the magnetite has a relatively homogeneous FeO* content between 72.4 and 76.1 wt% and TiO_2 contents around 1.4 wt%. The remaining high abundance elements in the magnetites are Al_2O_3, Cr_2O_3 and MgO. The magnetites vary by up to a factor of 2.8 in Cr_2O_3 contents at a single pressure and temperature.

In experiments conducted at NNO at 200 and 500 MPa, the oxide phase that is stable is a chromite spinel. In all experiments containing large enough chromite spinels to be analyzed by microprobe, the calculated mode of the mineral was <1 % by mass. The Cr# ($Cr_2O_3/[Cr_2O_3 + Al_2O_3]$, molar) varies from 0.742 to 0.683 in 500 MPa experiments but does not vary systematically with temperature. Of the five experiments at NNO which contain chromite spinel, 4 of these experiments used powdered rock as starting material and it should be noted that the rock sample of 85-41c does contain high Cr# chromites. It is possible that the chromites in the experiments are partially equilibrated remnant mineral fragments from the rock sample. However, due to the extremely small volume of the chromite phase, partial equilibrium for this phase will not effect the chemistry of the other phases.

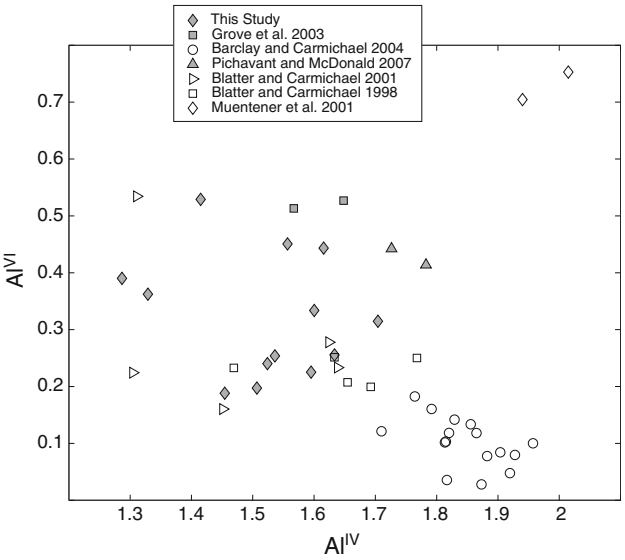

Fig. 4 Calculated Al site partitioning in experimental amphiboles crystallized from primitive arc magma starting materials from this study and the experimental literature. For these high thermodynamic variance systems there is no observable trend with tetrahedral coordinated Al vs. octahedral coordinated Al. Site assignments are calculated with the algorithm of Leake et al. (1997) on a 23 oxygen basis

Amphibole

At 200 MPa, the first amphibole to crystallize has 9.9 % Al_2O_3 while the first-appearing amphibole at 500 MPa contains 12.5 % Al_2O_3. The first amphibole at 800 MPa has a higher Mg# (81.7) than the lower-pressure amphiboles but also contains lower Al_2O_3 (11.9 wt%). The 200 MPa amphiboles have the lowest Al_2O_3 because they were crystallized at the lowest pressure and co-precipitated with plagioclase, from liquids depleted in an Al-rich plag component. There is also no systematic variation of tetrahedrally coordinated Al (Al^{IV}) with octahedrally coordinated Al (Al^{VI}) observed in the first-appearing amphiboles. We compare our amphibole data to that of the literature in Fig. 4. Amphiboles that occur in high thermodynamic variance systems (i.e., the amphibole coexists with only a few other phases, but the system has many components) display no relationship between Al^{IV} and Al^{VI}. This is in contrast to amphiboles that coexist with many other phases (i.e., low variance systems, Hammarstrom and Zen (1986); Johnson and Rutherford (1989); Schmidt (1992) where there are pressure sensitive relationships between these two crystal-chemical variables).

Amphibole composition and the temperature of its first appearance are sensitive to the Fe^{2+}/Fe^{3+} ratio in the melt. Experiments at higher oxygen fugacities crystallize a more magnesium-rich amphibole for a given pressure and temperature than those at NNO. Our experiments were conducted at NNO across all pressures, RRO for some 200 MPa experiments and some at NNO+3 at 500 MPa. The Mg# of the first amphibole to crystallize is greater in the oxidized experiments (77.0 vs. 74.7 at 200 MPa, and 81.5 vs. 79.9 at 500 MPa). The compositions of the amphiboles in our experiments are on the border between compositional regimes and are classified as a mix of pargasite, magnesio-hastingsite, magnesio-hornblende, and tschermakite (Leake et al. 1997). For simplicity we refer to this phase as amphibole in this paper.

In the H_2O-undersaturated experiments, amphibole is stabilized to higher temperatures, however the amphibole in the H_2O-undersaturated experiments has a lower Mg#, because the liquidus is at a higher temperature for the primitive magnesian andesite under H_2O-undersaturated conditions (experiments 41c-106, 117, and 118, Table 2).

Liquid

The liquid compositions vary from 57.8 % SiO_2 in near liquidus experiments to 65.4 % SiO_2 in the lowest temperature experiment at 200 MPa for the primitive magnesian andesite composition, normalized anhydrous (Fig. 5). The suppression of plagioclase crystallization in the higher pressure experiments allows the liquids to continue to increase in Al_2O_3 content down temperature, and for similar MgO contents (3 wt% MgO), the 500 and 800 MPa experiments have up to 19.3 % Al_2O_3 vs. about 17.7 wt% for the 200 MPa experiments (Fig. 5), which are saturated with plagioclase.

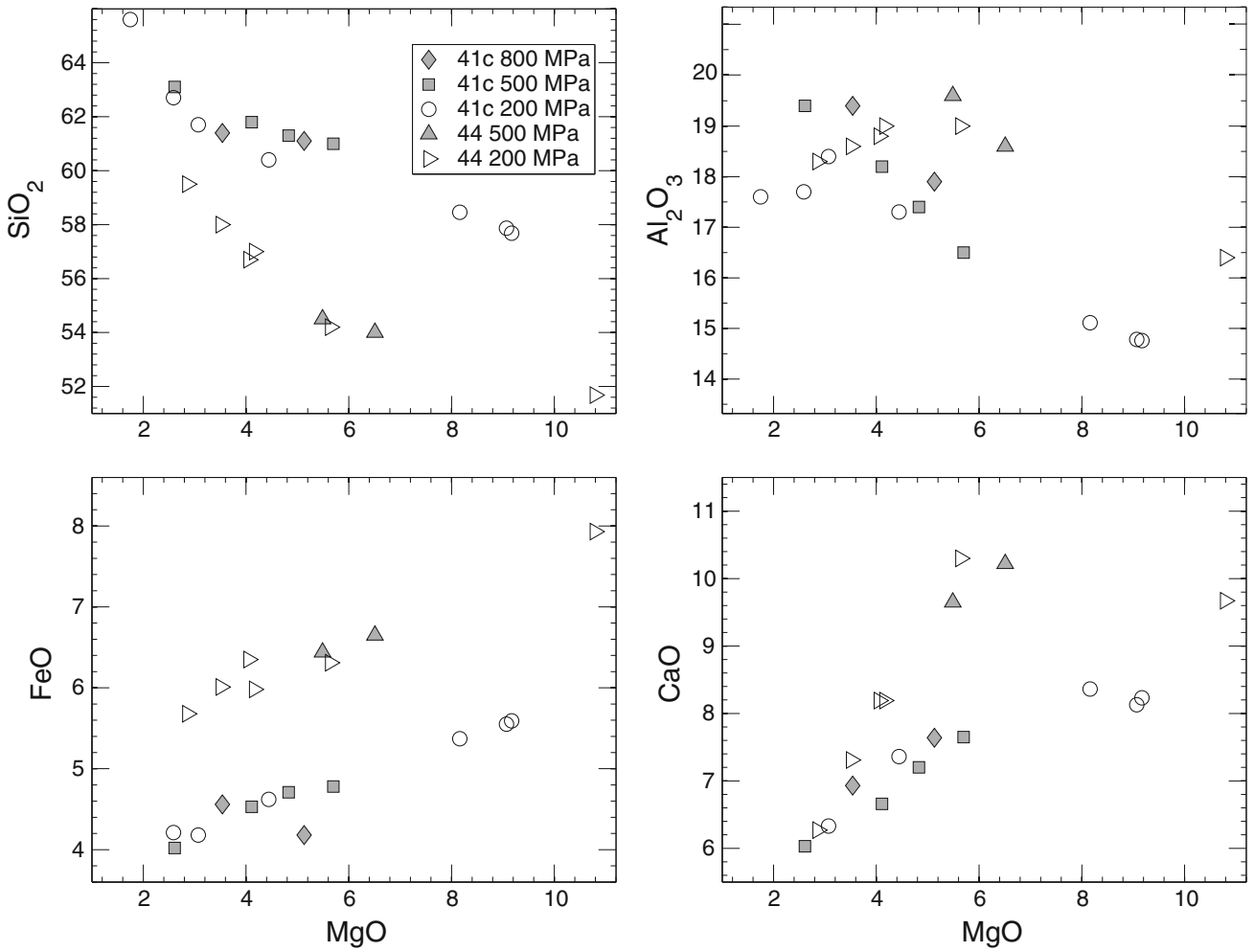

Fig. 5 Variation diagrams showing the compositions of experimental glasses, with the composition normalized anhydrous. Crystallization over a wide range of pressure produces indistinguishable compositions in major elements, except for low values of MgO and high Al_2O_3 where the presence/absence of plagioclase greatly affects the Al_2O_3 content (see section "Discussion")

Discussion

Effects of P, H_2O on phase equilibria

The phase appearance sequence and crystallization temperatures for the primitive magnesian andesite H_2O-saturated experiments change in response to variations in pressure (i.e., total dissolved H_2O content). With increasing pressure, the amphibole-in curve increases in temperature and the liquidus decreases, and thus the difference in temperature between the first amphibole and the liquidus monotonically decreases with increasing P_{H_2O} over the pressure range investigated here. Olivine is the liquidus silicate phase at all pressures. At 200 MPa, there is a 90 °C gap between the disappearance of olivine and the appearance of amphibole, and a 220 °C gap between amphibole first appearance and the liquidus. At 500 MPa, the disappearance of olivine in the crystallization sequence coincides with the appearance of amphibole, and at 800 MPa olivine and amphibole coexist (Fig. 3). The 500 MPa coexistence defines the low-pressure end of a narrow field of P-T space where both amphibole and olivine are coexisting, though this is a reaction relationship (Fig. 6).

The appearance temperature of clinopyroxene drops between 0.1 and 200 MPa by about 100 °C but remains relatively constant until at least 800 MPa. The temperature difference between the orthopyroxene-in curve and the liquidus increases between 0.1 and 500 MPa; this is the opposite sense to the behavior of amphibole. Between 500 and 800 MPa, the temperature difference between opx appearance and the liquidus decreases, similar to the slope of the amphibole-in curve. At 0.1 MPa opx crystallizes before cpx, and at 200 and 500 MPa, opx first crystallizes after the first appearance of cpx. This crystallization sequence occurs because the effect of increasing P_{H_2O} is to

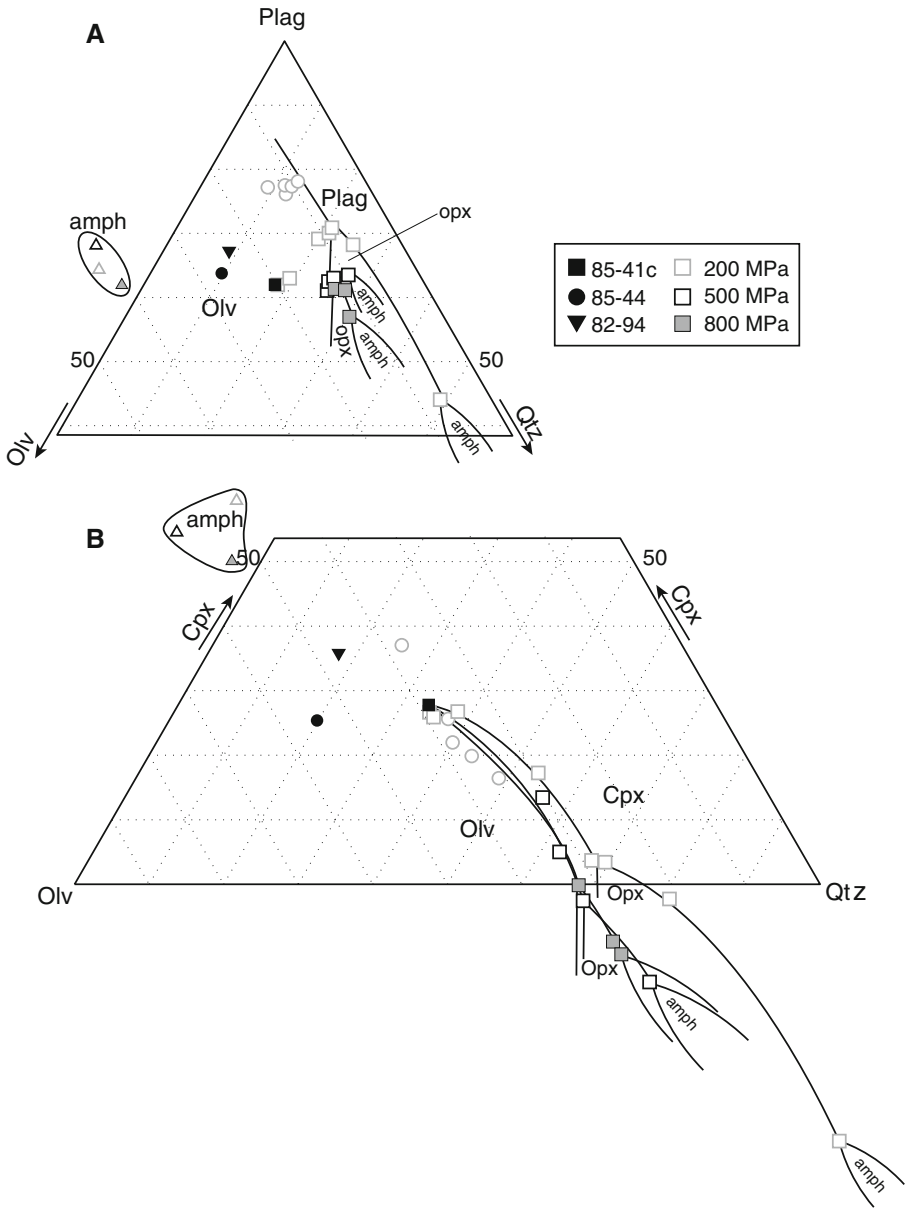

Fig. 6 Pseudo-ternary *diagrams* showing experimental liquid compositions recalculated into their respective mineral components in oxygen units following the method of Tormey et al. (1987). Also shown are the compositions of the primitive lavas from the Mt. Shasta region and amphiboles from our experiments. Notice that the amphibole stability field is a distributary reaction point. **a** Projection from the cpx apex into the Oliv-Plag-Qtz plane. Notice the large difference between the liquid compositions in equilibrium with amphibole between 200 and 500 MPa due to the switching of amphibole and plagioclase in the crystallization sequence. **b** Projection through the plag apex into the Oliv-Cpx-Qtz plane. Notice that the opx-in point does not vary much with pressure due to the counteracting effects of increased pressure and increased water content

expand the olivine primary stability field (Kushiro 1969). The olivine-orthopyroxene reaction boundary moves to higher SiO_2 contents with increasing P_{H_2O}, and this change is most dramatic between 0.1 and 200 MPa. From 200 to 800 MPa the boundary does not shift. The effects of increasing H_2O in the melt (serving to expand the boundary) and increased pressure (causing the boundary to shrink) apparently cancel each other out (Fig. 6). The crystallization sequence between opx and cpx at 800 MPa has not been determined.

Plagioclase saturation has only been found in experiments at 200 MPa, and there is a 170° drop in the appearance temperature compared to 1-atm crystallization experiments (Grove et al. 2003). The lowest experimental temperature at 500 MPa is 945 °C, and the liquid contains 19.3 wt% Al_2O_3, normalized anhydrous, and this liquid is not saturated with plagioclase at $P_{H_2O} = P_{tot}$ conditions. At 200 MPa plagioclase first crystallized at 1,000 °C, from a liquid with 17.7 wt% Al_2O_3. The drop in plagioclase appearance temperature from 1-atm to 500 MPa at H_2O-saturated conditions is at least 265 °C in the primitive magnesian andesite composition.

High-Mg andesite liquid line of decent at 200–800 MPa

Because the near liquidus phase assemblages for H_2O-saturated primitive magnesian andesite are similar from 200–800 MPa (Olivine-Cpx-Opx), the major element variation diagrams show that the liquids evolve in very similar fashion for the early part of the crystallization sequence at

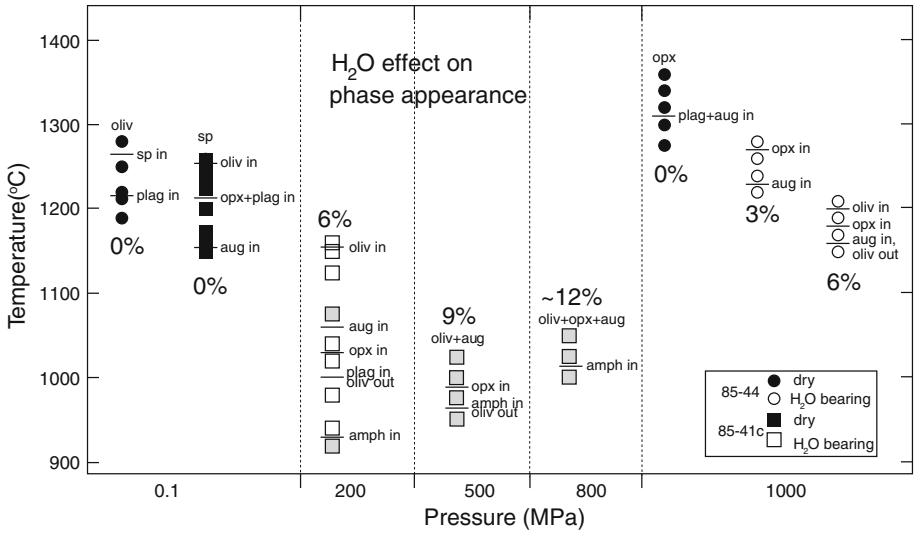

Fig. 7 Experimental crystallization sequences for the primitive magnesian andesite water-saturated compared to the experiments of Baker et al. (1994) on the basaltic andesite at various H_2O contents. Note the very large temperature difference and different phase assemblages in the basaltic andesite and primitive magnesian andesite at high pressure and varying H_2O content. Both magmas have very similar phase assemblages and mineral appearance at 1-atm but are vastly different dry versus H_2O saturated at high pressure. Numbers next to the columns represent the amount of H_2O in wt% dissolved in the liquid. *Gray squares* denote the H_2O-saturated experiments from this study, white squares are from Grove et al. (2003)

all pressures (Fig. 5). Therefore, major element compositional variations are not diagnostic for determining the pressure of crystallization for H_2O-rich primitive arc magmas (>5 wt% MgO) that fractionate over a large range of crustal depths. For primitive high-Mg andesites and basaltic andesites, polybaric magmatic fractionation and evolution that have been seen at magmatic arcs (Prouteau and Scaillet 2003) have similar major element signatures as ponding and differentiation at a single depth in a fixed magma chamber (Sherrod et al. 2008; Barclay et al. 1998). At lower MgO contents, and more evolved compositions, there are significant differences between experimental liquids produced by crystal fractionation at various crustal depths, particularly in their Al_2O_3 variations. It has been shown that the crystallization of plagioclase is highly dependent on H_2O content (Sisson and Grove 1993; Panjasawatwong et al. 1995) and suppressed to very low temperature at high dissolved H_2O contents. All of our experiments are done at high-H_2O contents and thus the plagioclase appearance shifts from high to low temperature at low and high pressures, respectively. There is a switch in the order crystallization between amphibole and plagioclase that takes place at about 300 MPa. Because of the aluminum-rich nature of plagioclase, crystal fractionation at shallow pressures (<300 MPa) will produce lower Al_2O_3 contents in residual liquids than higher pressure (>300 MPa) crystal fractionation at a given MgO content.

The liquid compositions for experiments are plotted in pseudo-ternary diagrams in Fig. 6. In the primitive magnesian andesite composition, olivine+opx+cpx saturation occurs at the same part of composition space from 200 to 800 MPa indicating that H_2O pressure does not change the compositional characteristics of the melt in equilibrium with these three phases. The olivine+opx+cpx saturation boundary is a reaction boundary down temperature and the liquids become enriched in the SiO_2 (Qtz) component with decreasing temperature. However, the appearance temperature of opx *does* vary with pressure, see Fig. 3. At 200 MPa the appearance of amphibole and the disappearance of olivine in the crystallizing assemblage are widely separated, and amphibole appears at a distributary point where opx+cpx+amph+liquid are stable. At 500 and 800 MPa, olivine stability terminates at a distributary reaction point where amphibole becomes stable on the dow n temperature side. The composition of the liquid at this reaction point varies systematically in the Olv-Cpx-Qtz projection, moving to less SiO_2 and less corundum normative compositions with increasing pressure (Fig. 6). In the Olv-Qtz-Plag projection, the 200 MPa liquid composition at the distributary reaction point is very Qtz-rich. The appearance of plagioclase before amphibole in the crystallization sequence drives the liquid away from the Plag apex. Above 300 MPa, amphibole appears before plagioclase, and the distributary point appears at more Plag-rich compositions (Fig. 6). In the Oliv-Cpx-Qtz projection, the distributary point systematically moves to lower Qtz values with increasing P_{H_2O}.

Effect of pressure on crystallization under anhydrous and hydrous conditions

The focus of this paper is on H_2O-saturated experiments at variable pressure and oxygen fugacity, but it is worth contrasting this work with the phase appearance sequence that would be expected if these magmas crystallized under anhydrous conditions. At near surface conditions, the crystallization sequence in the primitive magnesian andesite and basaltic andesite are very similar (Fig. 7). The phase equilibria of basaltic andesite 85-44 was investigated by Baker et al. (1994) at 1,000 MPa and variable H_2O content. The most noticeable difference is the increase in liquidus temperature and the absence of olivine as a liquidus phase at high pressures and low P_{H_2O}. The primitive magnesian andesite loses olivine as a liquidus phase by ~100 MPa and crystallizes opx followed closely by plagioclase. This crystallization sequence would most likely remain the same at 500 and 800 MPa, anhydrous, and the liquidus temperature would continue to climb to values that would approach or exceed the liquidus of 85-44 under anhydrous conditions (1,335 °C at 500 and 1,375 °C at 800 MPa). When we compare the experimental results to natural settings like Mt. Shasta, the mineral assemblage observed bears no resemblance to the dry phase appearances. The presence of olivine with Mg# of 81-83 and amphibole coexisting with primitive natural arc magmas is strong evidence for very high-pre-eruptive H_2O contents and H_2O-saturated conditions. In addition, the mineral assemblages in Mt. Shasta lavas record much lower temperatures for magmas in the crust (<1,000 °C with H_2O up to 11 wt%; Grove et al. 2005). At 800–1,000 MPa, there is a ~500 °C difference between the liquid of hydrous amphibole bearing magmas and an anhydrous magma of the same bulk composition.

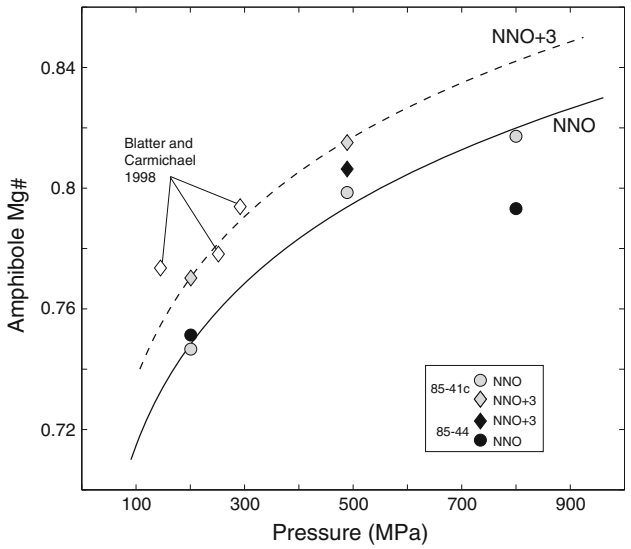

Fig. 8 Variation of the Mg# of the first amphibole to crystallize from a primitive arc magma with pressure. Diamonds are experimental amphiboles at approximately NNO+3, and *circles* are for experimental amphiboles at NNO. The range between amphibole Mg# between the primitive magnesian andesite and basaltic andesite starting materials is highlighted. *Black symbols* are experiments on the basaltic andesite and *grey symbols* are for the primitive magnesian andesite. Experiments from Blatter and Carmichael (1998) at conditions close to NNO+3 are shown for comparison. Plotted are two lines from our geobarometer-hygrometer, one for $\Delta NNO = 0$ (solid) and one for $\Delta NNO = 3$ (dotted)

Empirical amphibole barometry

Calibration of an amphibole Mg# geobarometer-hygrometer

The temperature difference between the liquidus and first appearance of amphibole in H_2O-saturated experiments decreases with increasing pressure, as has been noted by several authors in the past (Holloway and Burnham 1972; Helz 1973; Cawthorn and Ohara 1976; Anderson 1980). A direct result of this observation is that amphibole first crystallizes from higher Mg# liquids at higher P_{H_2O}. Thus, the Fe/Mg ratio of the first amphibole to crystallize changes along the phase stability boundary in P-T space due to the change in Mg# of the liquid, which in turn is dependent on overall crystallinity and relative proportions of other Fe-Mg phases. The magnitude of this change depends on the bulk composition of the system, and amphibole Mg# is also a function of f_{O_2}. We use the H_2O-saturated experiments on the primitive magnesian andesite and basaltic andesite compositions to calibrate the variation in Mg# in order to get a minimum pressure and f_{O_2} of crystallization of natural amphiboles.

A power law least squares fit was made using the experimental pressures and amphibole Mg#s, for experiments on the primitive magnesian andesite at NNO. The reason for choosing this mathematical formulation is that the Mg# of the first amphiboles to crystallize describes a nonlinear convex-up trend that tends to flatten out in pressure-Mg# space with increasing pressure. The flattening of the curve in pressure-Mg# space is because the amphibole stability curve becomes sub parallel with the liquidus curve at high pressures (Fig. 3). Experiments done at the NNO buffer contain amphiboles with lower Mg# than those produced at NNO+3 or RRO for a given pressure (Fig. 8), and thus an additional term is required in the fit. Because we have only done experiments at two different f_{O_2}s, this term is assumed to be linear over the range of conditions investigated for simplicity. The correction for f_{O_2} is expressed as a function of ΔNNO in log units. The regression produces the following expression:

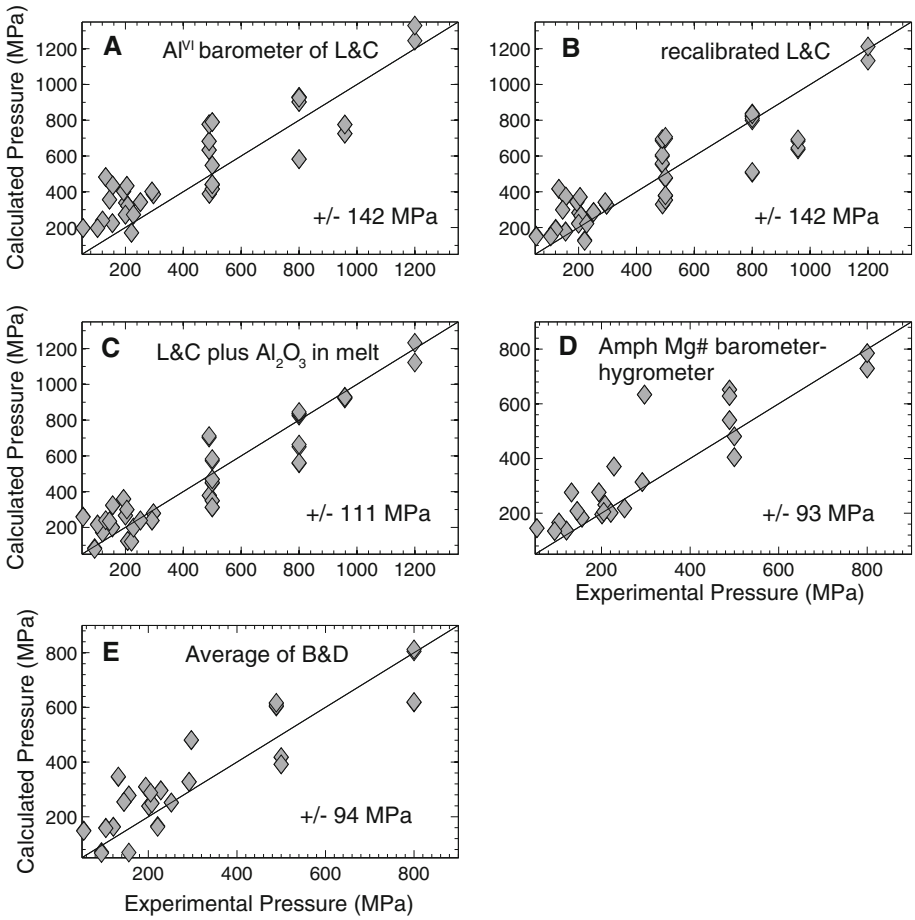

Fig. 9 Empirical amphibole barometer reproducibility of experimental pressures. Shown in each plot is the calculated pressure vs. the experimental pressure, and a 1:1 line. On each figure the standard deviation from the 1:1 line is shown. Experiments are from the sources listed in Table 4. **a** Al^{VI} barometer of Larocque and Canil (2010). **b** Adjusted barometer of Larocque and Canil (2010) including the calibration all of the experiments in Table 4. **c** The same as (b) but with an added term that accounts for the Al_2O_3 content of the melt in equilibrium with the amphibole, thus adjusting the values based on equilibrium non-pressure dependent Al^{VI} content in the amphiboles. **d** Calculated pressures using our Mg# barometer (Eq. (1)). Plotted are all of the experiments in Table 4 but excluding those not in the range of amphibole Mg# >74 and experimental pressures outside the 50–950 MPa range. **e** The average of the calculated pressures in plots (**b**) and (**d**), the independent empirical barometers

$$P_{H_2O}(\text{MPa}) = \left[\frac{\text{Mg\#}}{52.7} - 0.014 * \Delta\text{NNO}\right]^{15.12} \quad (1)$$

Only the composition of the first-appearing amphibole in a crystallization sequence at a given pressure is used in the calibration. This barometer is only to be used on amphiboles with Mg# between 74 and 84; below and above these values, the geometry of this curve is not meaningful. At higher pressures garnet may also become a stable crystallizing phase, which will affect the chemical composition and appearance of amphibole (Müntener et al. 2001; Alonso-Perez et al. 2009), and we do not recommend extrapolating this model beyond 950 MPa. Pressures calculated for experimental amphiboles not included in our regression are used to test the uncertainty of the barometer and are shown in Fig. 9d. The square root of the sum of the differences from the 1:1 line squared is ±93 MPa. However, the uncertainty is also subject to several other factors discussed below. There is a systematic offset in the barometer for amphiboles that are crystallized below ~180 MPa. This is an artifact of the geometry of the empirical curve used and shows the barometer-hygrometer performs most robustly at the 180–950 MPa range.

We made several conscious decisions in a consistent manner so that the barometer always gives a minimum pressure. Firstly, amphibole Mg# is a function of the parental magma composition. It is often difficult to asses the true parental melt composition of arc related volcanics because eruptive products often contain xenocrystic material and represent mixtures of two or more magma types. Our experiments and those of Grove et al. (2003) explored compositions that span a range of SiO_2 contents, including a primitive magnesian andesite, which is one of the most silica-rich mantle derived melt found at subduction zones

(Gaetani and Grove 2003). The increase in Mg# with pressure for the first amphibole to crystalize is greater for the higher SiO_2 primitive magnesian andesite composition than for the basaltic andesite composition, producing a steeper sloping curve in Fig. 8. This difference is negligible below 400 MPa (Fig. 8), but above that the barometer gives a *minimum* pressure only, assuming that primitive arc melts usually have similar or lower silica contents than the primitive magnesian andesite. As an example, using Eq. (1) and the amphibole in experiment 44–102 (a basaltic andesite starting material experiment), the calculated pressure is 412 MPa, compared to its actual pressure of 500 MPa.

Secondly, the hygrometer is calibrated using only H_2O-saturated experiments, but natural magmas are not always saturated in H_2O when crystallizing amphibole. If a parental magma is undersaturated with respect to dissolved H_2O, its liquidus temperature is higher, and the first amphibole to crystallize is thus lower in Mg# (Table 3, and Eggler 1972). In order to estimate the uncertainty in the barometer if the parental melt of the amphibole is undersaturated with respect to H_2O, we use the 3 experiments conducted at H_2O-undersaturated conditions that contain amphibole as test examples (41c-106,-117,-118; Table 2). Experiments 41c-106 and 41c-117 contain similar amounts of H_2O and were both run at about 500 MPa, but different f_{O_2}. The calculated P_{H_2O} for these two experiments using Eq. (1) are 242 and 352 MPa respectively. For experiment 41c-118, run at the same conditions but with even less dissolved H_2O, the pressure calculated from Eq. (1) is 215 MPa. The H_2O contents of these three mixed volatile experiments at 6–8 wt% H_2O are what one would expect for an andesitic liquid saturated with H_2O at 200–300 MPa. In this way it is evident the barometer-hygrometer is really a measure of P_{H_2O} and not P_{tot}. Because of these issues, the choices we have made in calibrating this equation with H_2O-saturated, high-SiO_2 starting materials consistently gives us the most conservative pressures from Eq. (1), and all the pressures derived from the barometer should be viewed as minimum crystallization pressures.

It is important to note that the first amphibole to crystallize at a given pressure usually occurs in an assemblage that is in equilibrium with >60 % melt by weight. Further crystallization at the same pressure would continue to crystallize amphibole, albeit with lower Mg#. Thus, the geobarometer-hygrometer presented here should only be applied to the most Mg-rich amphiboles in a given sample suite, and using amphiboles of a lower Mg# than the highest temperature amphiboles would again produce a minimum crystallization pressure.

Despite the somewhat large uncertainty in the pressure estimates, this barometer-hygrometer is convenient because it does not rely on the presence of many coexisting phases including uncommon accessory phases that fix the activities of various substitution components in the amphibole. The minimum error of ±93 MPa actually represents a great improvement for rocks that otherwise have few constraints on the depth of formation. Combining Eq. (1) with an independent aluminum-in-amphibole barometer as discussed in the following sections can help to estimate some of the uncertainty associated with unknown parental magma composition.

Calibration of an empirical Al^{VI} amphibole barometer

Larocque and Canil (2010) proposed an empirical geobarometer based on the calculated Al^{VI} content of igneous amphiboles in basalt and basaltic andesite systems. Using the experimental data available in the literature for basalt and basaltic andesite compositions (Müntener et al. 2001; Grove et al. 2005; Barclay and Carmichael 2004; Pichavant and MacDonald 2007), they showed an approximately linear relationship between Al^{VI} and pressure (Fig. 9). We extend this approach to higher silica compositions by adding our experimental amphiboles as well as those from other studies on andesitic liquids with high Mg# (Blatter and Carmichael 1998, 2001) (Table 4) to the calibration. The new regression shows that a clear relationship between pressure and Al^{VI} remains, but there is significant variability in the aluminum content at any single pressure. Much of this variability likely results from the large compositional range in the experimental liquids used in the calibration. On the one hand, that compositional variability in experimental liquids is good because it matches what is in nature, but on the other it makes a simple barometer like this harder to implement because of the multitude of variables it introduces. Ridolfi et al. (2010) have a more complicated barometer based on amphibole compositions, but it excludes much of the literature data. Figure 9a shows the calculated versus actual pressure for experimental amphiboles using the Larocque and Canil (2010) barometer, and the square root of the sum of the differences squared from the 1:1 line is 142 MPa. We have recalibrated this barometer using the same method of Larocque and Canil (2010) but with the added experiments, we obtained an updated equation:

$$P(\text{MPa}) = 1,675 * \text{Al}^{\text{VI}} - 48 \quad (2)$$

Where Al^{VI} is the calculated octahedrally coordinated Al atoms in the amphibole based on normalization to 23 oxygens. Equation (2) reproduces pressures that are slightly different than the equation of Larocque and Canil (2010) and have better reproducibility for the data, but with similar poor absolute uncertainty on the pressure (±142 MPa, Fig. 9b). The scatter in these plots results

Table 4 Comparison of empirical amphibole barometers

Source	P (MPa)	Mg#[a]	ΔNNO	Al^{VIb}	$Al_2O_3^c$	LC[d]	ΔP[e]	adj LC[f]	ΔP	$Al_2O_3^g$	ΔP	Mg#[h]	ΔP	ave[i]	ΔP
This study	800	81.5	0	0.334	19.31	582	−218	511	−289	562	−238	729	−71	620	−180
	800	81.9	0	0.529	19.52	930	130	838	38	836	36	785	−15	812	12
	489	80.9	0	0.362		633	144	559	70			652	163	606	117
	489	80.7	0	0.390		682	193	606	117			628	139	617	128
	489	79.9	0	0.443	19.36	777	288	695	206	711	222	540	51	617	128
	490	76.3	0	0.225	18.81	388	−102	329	−161	379	−111				
	500	78.1	3	0.451	17.62	790	290	707	207	582	82				
	500	79.8	3	0.254	17.97	439	−61	377	−123	350	−150				
	500	77.3	3	0.315	18.24	548	48	479	−21	452	−48				
	500	81.5	3	0.240	17.73	415	−85	354	−146	313	−187	481	−19	418	−82
	201	74.7	0	0.197		338	137	282	81			195	−6	239	38
	208	77.0	2	0.188	16.22	322	114	267	59	124	−84	231	23	249	41
	500	80.6	3	0.256	19.44	442	−58	380	−120	469	−31	405	−95	392	−108
G et al. (2003)	800	79.3	0	0.513	17.60	902	102	811	11	663	−137				
	800	78.2	0	0.527	19.68	926	126	834	34	846	46				
Ba and C (2004)	200	69.2	0.5	0.160	18.46	272	72	221	21	266	66				
	155	70.0	0.5	0.134	18.06	224	69	176	21	199	44				
	221	75.8	1.3	0.103	17.57	170	−51	125	−96	120	−101	201	−20	163	−58
	121	74.4	2	0.142	17.58	239	118	189	68	171	50	136	15	163	42
	104	75.2	1.8	0.118	18.52	197	93	150	46	215	111	166	62	158	54
	94	75.1	3	0.028	18.30	36	−58	−1	−95	79	−15	135	41	67	−27
	54	74.5	1.7	0.118	19.06	197	143	150	96	258	204	145	91	148	94
P and M (2007)	958	81.0	2.1	0.414	22.61	725	−233	645	−313	931	−27				
	958	81.8	2.2	0.442	22.10	776	−182	693	−265	928	−30				
Bl and C (2001)	194	77.0	0.81	0.233	18.43	402	208	343	149	359	165	276	82	310	116
	228	79.1	1.64	0.160	17.61	272	44	221	−7	198	−30	371	143	296	68
	297	81.2	0.57	0.224	17.57	386	89	328	31	279	−18	634	337	481	184
	132	76.9	0.62	0.278	16.19	482	350	417	285	240	108	276	144	347	215
Bl and C (1998)	292	79.4	3.13	0.233	16.93	401	109	342	50	239	−53	314	22	328	36
	205	77.1	3	0.250	17.41	433	228	371	166	300	95	205	0	288	83
	156	76.6	3	0.251	17.69	435	279	373	217	324	168	183	27	278	122
	252	77.8	3.49	0.199	17.47	342	90	286	34	239	−13	218	−34	252	0
	145	77.4	3.17	0.207	17.28	356	211	299	154	234	89	208	63	254	109
M et al. (2001)	1200	75.2	0	0.705	20.19	1245	45	1133	−67	1122	−78				
	1200	74.1	0	0.753	20.79	1330	130	1213	13	1233	33				

[a] Mg# of experimental amphibole

[b] Al^{VI} calculated by method of Leake et al. (1997)

[c] This is the Al_2O_3 of the melt in equilibrium with the amphibole, with the melt normalized anhydrous to 100 % total

[d] Barometer of Larocque and Canil (2010): Al^{VI}=0.056*P+0.008 (P is in kbar not MPa)

[e] Difference in MPa of calculated pressure from previous column and the experimental pressure

[f] A new barometer calibrated by the same method of Larocque and Canil (2010) but adding ours and experiments from Barclay and Carmichael (2004); Blatter and Carmichael (1998, 2001) to the calibration

[g] New calibration following the method of Larocque and Canil (2010) but with a term added to account for non-P dependent Al^{VI} content

[h] Mg# barometer of this paper (Eq. (1))

[i] Average pressure from the adjusted LC and Mg# barometers

from complicated amphibole compositional variability including non-pressure dependent Al^{VI} content and highly variable Ti contents.

We added a term to the linear regression to adjust the pressure based on aluminum content in the melt, and this improves the ability of the regression to recover

experimental pressures (± 111 MPa 67 % confidence interval, Fig. 9c). However, it is difficult to estimate the aluminum content of the melt in equilibrium with amphibole in most natural cases, and so while the additional parameter improves the pressure estimates, it is more difficult to implement. The fact that including a term for Al_2O_3 content of parental melts improves the fit highlights that some of the uncertainty in the use of a strictly empirical Al^{VI} barometer is related to non-pressure dependent, mineral/liquid partitioning of Al^{VI} content in amphibole.

The Mg# barometer should always be used with the most Mg-rich amphibole of a given rock suite to estimate the pressure; however, this is not guaranteed to be the most Mg-rich amphibole that was crystallized from a parental magma because of down temperature reaction removing primitive amphibole, metamorphic redistribution of Fe-Mg in plutonic rocks, or under sampling. Thus, we would expect some underestimation of the pressure using this barometer. Conversely, use of the Al^{VI} barometer on an amphibole with lower Mg# than the most Mg-rich amphibole possible for a particular bulk composition will overestimate the pressure, because of the increase in Al_2O_3 content in the melt from some excessive crystallization of phases in which Al_2O_3 is incompatible. Averaging the Mg# barometer and the Al^{VI} barometer, and applying them to the same suite of rocks can help with the non-uniqueness of each barometer (± 94 MPa, Fig. 9e). Although neither the Mg# hygrometer or Al^{VI} barometer presented here are perfect, they are both independent and complement each other and are great improvements for rocks that otherwise have few constraints on their depth (pressure) of origin.

In order to apply the Mg# barometer-hygrometer, we stress that a rigorous petrologic approach needs to be implemented. The association of amphibole with olivine and/or pyroxene, and the relation of the amphibole to the crystallization of plagioclase need to be considered when applying this technique for pressure estimates. For instance, if pressure estimates of >300 MPa from this barometer-hygrometer are obtained, there should be clear corroborating textural evidence for amphibole as an early crystallizing phase appearing after or co-precipitating with olivine, opx and/or cpx and before plagioclase appearance. It must also be clear that the amphiboles were not affected by post-crystallization processes such as low temperature metamorphic reactions that can create very Mg-rich rims on amphiboles (Tiepolo et al. 2011). In addition, normal or oscillatory zoned amphiboles are common in igneous rocks, because the Mg# barometer-hygrometer only applies to the most Mg-rich amphiboles that crystallize at high temperatures and H_2O contents, only the most Mg-rich compositions from primary igneous amphiboles should be used to estimate pressure.

Example of near liquidus amphibole crystallization at Mt. Shasta, CA

High-Mg amphibole antecrysts are present in mixed andesites erupted from Mt. Shasta, CA. These crystals are typically overgrowths on magnesian olivine and cpx (Grove et al. 2003), both of which are early crystallizing phases from a hydrous primitive magnesian andesite or basaltic andesite (Fig. 3). The amphiboles reported in Grove et al. (2003, 2005) (Fig. 10) range in their Mg# from 57.0 to 83.3 and in Al^{VI} content from 0.164 to 0.313. These amphiboles crystallized from liquids similar to the ones used in the experiments and the amphiboles from the 200, 500 and 800 MPa are plotted along with the amphiboles found in the Shasta lavas (Fig. 10). There is good evidence from amphibole composition that Mt. Shasta lavas were crystallizing at lower crustal depths and contained high H_2O contents. We can also estimate an oxygen fugacity for these Mt. Shasta eruptive products as an average of NNO+0.5 from measurements of coexisting oxides from 32 separate lava flows from the Mt. Shasta stratocone (Grove et al. 2005). Using Eq. (1) to estimate the P_{H_2O} gives a range from 276 to 948 MPa for amphiboles with Mg# 73 or greater (Table 5). This implies that these antecrysts came from magmas at or near the Moho underneath Mt. Shasta (Zucca et al. 1986).

Evidence from amphibole for high magmatic H_2O in primary magmas from subduction zones

The amphibole coexistence with olivine and high-Mg#s of the amphibole in the Mt. Shasta andesites requires these

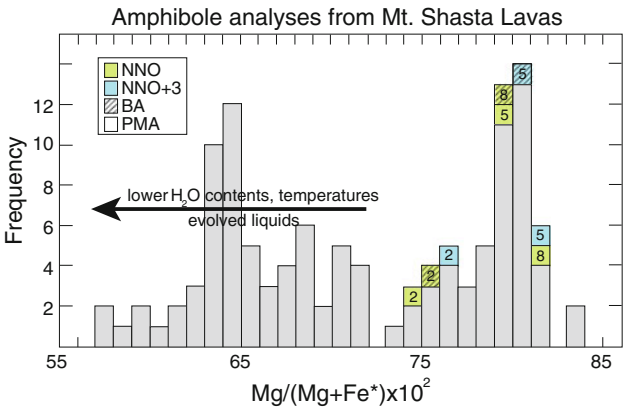

Fig. 10 Histogram of amphibole phenocryst Mg#s from Mt. Shasta lavas from Grove et al. (2005). Also plotted are the experimental amphiboles we have produced in this study. Each experimental amphibole is labeled with its pressure in kbar, and the estimated H_2O content necessary to precipitate it. Experimental amphiboles range in f_{O_2} and are both primitive magnesian andesite and BA. The high-Mg# peak in the Mt. Shasta region amphiboles is proposed to represent deep and H_2O-rich fractionation

Table 5 Calculated crystallization pressures of Mt. Shasta high-Mg# amphiboles

Calculated Pressures						
Sample	Amph Mg#	ΔNNO	Al^{VI}	adj LC	Mg#	average
82-85	83.3	0.5	0.164	226	949	588
82-85	81.3	0.5	0.194	277	656	467
82-88a	76.8	0.5	0.195	278	276	277
85-59	78.2	0.5	0.242	358	363	361
83-56	80.0	0.5	0.313	476	514	495
96-5	80.0	0.5	0.245	362	514	438
96-11b	81.2	0.5	0.309	469	644	556
97-1f	79.7	0.5	0.244	361	485	423

All pressures in MPa, amphibole compositions and f_{O_2} from Grove et al. (2005)

magmas were H_2O saturated at depth. Using the pressures determined from the Mg# of the amphiboles, and because of the very narrow temperature stability window for amphibole, we know that the conditions of crystallization must be between 915–1,050 °C and 276 to 948 MPa. But what is the H_2O content of such magmas? Hamilton et al. (1964) determined the maximum H_2O solubility of a Mt. Hood andesite composition equilibrated with a pure H_2O fluid from 100 to 500 MPa to be 4.5 and 10 wt%, respectively. More recent measurements on a Mt. Unzen andesite composition equilibrated with a pure H_2O fluid determined the solubility of H_2O to be 5.5 and 10 wt% at 200 and 500 MPa (Botcharnikov et al. 2006). We compared these experimental results to the H_2O solubility-pressure curves from Newman and Lowenstern (2002) for basalt and rhyolite magmas. Although the model of Newman and Lowenstern (2002) is simplified and does not cover magmas of intermediate silica content, we found that the VolatileCalc software of Newman and Lowenstern (2002) reproduced the experimental andesite solubilities of H_2O well when an average of 75 % basalt and 25 % rhyolite H_2O solubilities at 1,000 °C was used. At the upper pressure limit of VolatileCalc, the H_2O solubility curves for basalt and rhyolite are approximate linear and we have extrapolated them linearly to 950 MPa and obtain a result of 14–15 wt% H_2O in saturated andesite at 950 MPa. These H_2O contents are significantly higher than the amounts preserved in melt inclusions in olivine phenocrysts (Anderson 1974; Ruscitto et al. 2011; Sisson and Layne 1993). Even if the high Mg# amphiboles come from oxidized magmas ($f_{O_2} = NNO + 3$), these igneous amphiboles with high Mg# require pre-eruptive H_2O contents that exceed 12 wt% and crystallization pressures that extend at least to the base of the crust.

The experiments presented in this paper allow a new upper limit to be placed on magmatic H_2O contents in the Cascade arc. Using our experimental results to link amphibole composition to temperature of crystallization, and using extrapolated H_2O solubilities from VolatileCalc, the high-Mg# amphibole antecrysts of Mt. Shasta lavas record pre-eruptive temperatures of 1,050 °C at lower crustal depths with H_2O contents that are at 14 wt% (Fig. 11).

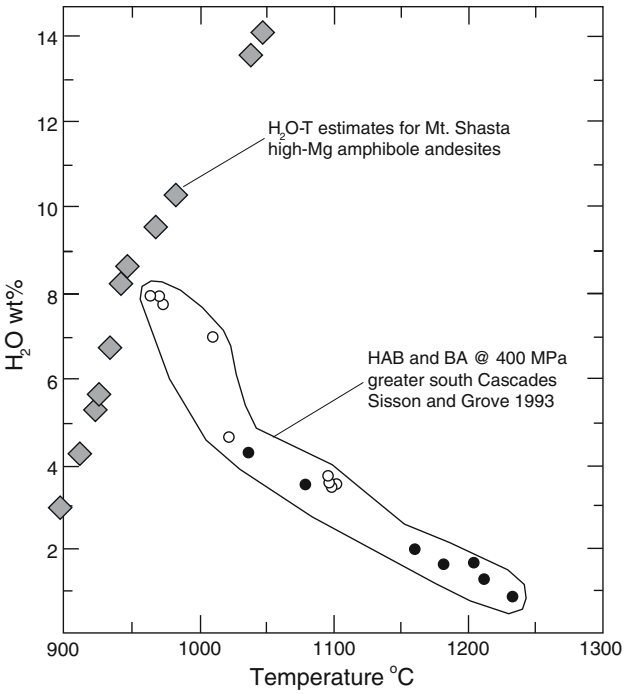

Fig. 11 Dissolved H_2O content and magmatic temperatures are estimated for the parental magmas crystallizing high-Mg# amphiboles in Mt. Shasta lavas modified after Grove et al (2012). Experimental amphibole Mg# and temperatures were used to make a calibration curve to determine the temperature of parental magma to the Shasta amphiboles in Table 5. Pressure estimates come from the amphibole Mg# barometer calibrated for these specific magmas. Pressure estimates were then converted to H_2O contents assuming water saturation and using a mixture of 75 % basalt and 25 % rhyolite solubilities at 1,000 °C from VolatileCalc. The trend defined by the Mt. Shasta samples (*diamonds*) defines an H_2O-saturated crystallization trend of magmas as they ascend through the crust, so the high-H_2O, high T samples are the deepest and the low H_2O and low T are the shallowest. The HAB and BA trend of S. Cascades lavas is from Sisson and Grove (1993) and represents variable melting processes that produce variable water contents for mantle derived melts

The trend defined by the Mt. Shasta amphibole antecrysts in Fig. 11 is evidence preserved in Mt. Shasta lavas that fractional crystallization of primitive lavas occurs over a great depth range extending from the base of the crust to magmas that pond near the base of the Mt. Shasta edifice. The presence of multiple compositions of these amphiboles in single lava flows suggests magmas are mixed throughout the crustal column just prior to eruption. Grove et al. (2005) suggest that vapor saturation of high-H_2O primitive magmas near the base of the crust is the trigger for mixing of lavas. These deep, high-H_2O magmas are mingled with lower-pressure evolved liquids and degassed shallower products of fractional crystallization. Thus, the erupted andesite collected products of vapor-saturated crystallization over a range of depths.

Studies of basalts and basaltic andesites from the South Cascade region have revealed evidence for variable pre-eruptive water contents and temperatures that range from 8 to <1 wt% H_2O and 1,000–1,250° (Fig. 11) using olivine-liquid and plagioclase-liquid equilibrium thermometer/hygrometers (Sisson and Grove 1993). These variations in water content may represent primary features of the melt generation processes that are taking place in the mantle at subduction zones (Grove et al. 2002). The high-T, low-H_2O end of the spectrum represents 'dry' adiabatic decompression melting of mantle peridotite that is convecting into the wedge corner. The low–T, high H_2O end of the spectrum is being generated by flux melting of the mantle wedge that occurs when H_2O is added at the slab–wedge interface, leading to reactive porous flow melting that is controlled by the inverted temperature gradient in the wedge. These very high H_2O contents and cooler melts may have undergone reactive crystallization with the shallow mantle lithosphere above the hot core of the mantle wedge resulting in increased H_2O contents and cooler mantle temperatures (Grove et al. 2003).

The trend defined by polybaric H_2O-saturated crystallization in the melt conduit beneath Mt. Shasta (diamonds in Fig. 11) intersects the trend defined by the South Cascades high-alumina basalts and basaltic andesites (circles in Fig. 11) at about 450 MPa, which is to be expected because the S. Cascades magmas become vapor saturated at this pressure. The two trends come from independent hygrometers. The Mt. Shasta trend defined by the amphibole antecrysts extends the range of magmatic H_2O contents in the South Cascades region to significantly higher values.

These high H_2O contents are not the first to be inferred from petrologic evidence. Indeed, Carmichael (2002) proposed that the lavas from the Mexican Volcanic Belt contained up to 16 wt% pre-eruptive H_2O. Carmichael (2002) also suggested that these lavas would become H_2O saturated at significant depth and remain water saturated as they ascend through the crust. They could initially contain higher H_2O contents than the phenocrysts that crystallized at shallower depths record. Ridolfi et al. (2010) infer lower crustal depths of crystallization for amphiboles at Mount St. Helens, Redoubt, El Reventador, and Soufriere Hills, which would require high H_2O contents to crystallize. Lavas that are erupted on the surface may experience complicated ascent (decompression) crystallization and mixing paths to their site of eruption (Blundy et al. 2006), and experiments like the ones presented here provide critical evidence for understanding the ultimate fate of H_2O-rich magmas between their source regions in the mantle and the erupted products we are privileged to study.

Acknowledgments The Authors would like to thank two anonymous reviewers for their constructive comments that improved the manuscript. In addition, experimental assistance from S. Feig at the University of Hannover for the IHPV experiments was invaluable. We acknowledge support from the National Science Foundation (EAR-0538179 and EAR-1118598).

References

Allen JC, Boettcher AL (1983) The stability of amphibole in andesite and basalt at high-pressures. Am Mineral 68(3-4):307–314

Alonso-Perez R, Müntener O, Ulmer P (2009) Igneous garnet and amphibole fractionation in the roots of island arcs: experimental constraints on andesitic liquids. Contrib Miner Petrol 157:541–558. doi:10.1007/s00410-008-0351-8

Anderson AT (1974) Evidence for a picritic, volatile-rich magma beneatch Mt. Shasta, CA. J Petrol 15(2):243–267

Anderson AT (1980) Significance of hornblende in calc-alkaline andesites and basalts. Am Mineral 65(9–10):837–851

Armstrong JT (1995) CITZAF—A package of correction programs for the quantitative electron microbeam X-ray-analysis of thick polished materials, thin-films, and particles. Microbeam Anal 4(3):177–200

Ayers JC, Brenan JB, Watson EB, Wark DA, Minarik WG (1992) A new capsule technique for hydrothermal experiments using the piston-cylinder apparatus. Am Mineral 77(9–10):1080–1086

Baker MB, Grove TL, Price R (1994) Primitive basalts and andesites from the Mt. Shasta region, N. California: products of varying melt fraction and water content. Contrib Miner Petrol 118:111–129. doi:10.1007/BF01052863

Barclay J, Carmichael I (2004) A hornblende basalt from western Mexico: water-saturated phase relations constrain a pressure-temperature window of eruptibility. J Petrol 45(3):485–506. doi:10.1093/petrology/egg091

Barclay J, Rutherford MJ, Carroll MR, Murphy MD, Devine JD, Gardner J, Sparks RSJ (1998) Experimental phase equilibria constraints on pre-eruptive storage conditions of the Soufriere Hills magma. Geophys Res Lett 25:3437–3440. doi:10.1029/98GL00856

Benne D, Behrens H (2003) Water solubility in haplobasaltic melts. Eur J Mineral 15:803–814. doi:10.1127/0935-1221/2003/0015-0803

Berndt J, Liebske C, Holtz F, Freise M, Nowak M, Ziegenbein D, Hurkuck W, Koepke J (2002) A combined rapid-quench and H_2-membrane setup for internally heated pressure vessels: description and application for water solubility in basaltic melts. Am Mineral 87(11-12):1717–1726

Blatter DL, Carmichael ISE (1998) Plagioclase-free andesites from Zitácuaro (Michoacán), Mexico: petrology and experimental constraints. Contrib Miner Petrol 132:121–138. doi:10.1007/s004100050411

Blatter DL, Carmichael ISE (2001) Hydrous phase equilibria of a Mexican high-silica andesite: a candidate for a mantle origin. Geochim Cosmochim Acta 65:4043–4065. doi:10.1016/S0016-7037(01)00708-6

Blundy J, Cashman K, Humphreys M (2006) Magma heating by decompression-driven crystallization beneath andesite volcanoes. Nature 443:76–80. doi:10.1038/nature05100

Botcharnikov RE, Behrens H, Holtz F (2006) Solubility and speciation of c-o-h fluids in andesitic melt at t = 1100–1300 degrees c and p = 200 and 500 mpa. Chem Geol 229:125–143

Boyd FR, England JL (1960) Apparatus for phase-equilibrium measurements at pressures up to 50 kilobars and temperatures up to 1,750 °C. J Geophys Res 65:741–748. doi:10.1029/JZ065i002p00741

Carmichael I (2002) The andesite aqueduct: perspectives on the evolution of intermediate magmatism in west-central (105–99°W) Mexico. Contrib Miner Petrol 143:641–663. doi:10.1007/s00410-002-0370-9

Cawthorn RG, Ohara MJ (1976) Amphibole fractionation in calc-alkaline magma genesis. Am J Sci 276(3):309–329

Davidson J, Turner S, Handley H, MacPherson C, Dosseto A (2007) Amphibole "sponge" in arc crust? Geology 35:787–+. doi:10.1130/G23637A.1

Eggler DH (1972) Amphibole stability in H_2O-undersaturated calc-alkaline melts. Earth Planet Sci Lett 15:28–+. doi:10.1016/0012-821X(72)90025-8

Gaetani GA, Grove TL (2003) Experimental constraints on melt generation in the mantle wedge. AGU Monograph 138(138):107–134

Grove TL, Donnelly-Nolan JM (1986) The evolution of young silicic lavas at medicine lake volcano, California: implications for the origin of compositional gaps in calc-alkaline series lavas. Contrib Miner Petrol 92:281–302. doi:10.1007/BF00572157

Grove TL, Donnelly-Nolan JM, Housh T (1997) Magmatic processes that generated the rhyolite of glass mountain, medicine lake volcano, N. California. Contrib Miner Petrol 127:205–223. doi:10.1007/s004100050276

Grove TL, Parman SW, Bowring SA, Price RC, Baker MB (2002) The role of an H_2O-rich fluid component in the generation of primitive basaltic andesites and andesites from the Mt. Shasta region, N California. Contrib Miner Petrol 142:375–396

Grove TL, Elkins-Tanton LT, Parman SW, Chatterjee N, Müntener O, Gaetani GA (2003) Fractional crystallization and mantle-melting controls on calc-alkaline differentiation trends. Contrib Miner Petrol 145:515–533. doi:10.1007/s00410-003-0448-z

Grove TL, Baker MB, Price RC, Parman SW, Elkins-Tanton LT, Chatterjee N, Müntener O (2005) Magnesian andesite and dacite lavas from Mt. Shasta, northern California: products of fractional crystallization of H_2O-rich mantle melts. Contrib Miner Petrol 148:542–565. doi:10.1007/s00410-004-0619-6

Grove TL, Till CB, Krawczynski MJ (2012) The role of H_2O in subduction zone magmatism. Ann Rev Earth Planet Sci 40:413–439

Hamilton DL, Burnham CW, Osborn EF (1964) The solubility of water and effects of oxygen fugacity and water content on crystallization in mafic magmas. J Petrol 5(1):21–39

Hammarstrom JM, Zen EA (1986) Aluminum in Hornblende—an empirical igneous geobarometer. Am Mineral 71(11–12):1297–1313

Helz RT (1973) Phase relations of basalts in their melting range at $P_{H_2O} = 5$ kbar as a function of oxygen fugacity .1. Mafic phases. J Petrol 14(2):249–302

Helz RT (1976) Phase relations of basalts in their melting ranges at $P_{H_2O} = 5$ kbar. 2. Melt compositions. J Petrol 17(2):139–193

Hidalgo PJ, Rooney TO (2010) Crystal fractionation processes at Baru volcano from the deep to shallow crust. Geochem Geophys Geosys 11. doi:10.1029/2010GC003262

Holloway JR, Burnham CW (1972) Melting relations of basalt with equilibrium water pressure less than total pressure. J Petrol 13(1):1–&

Johnson MC, Rutherford MJ (1989) Experimental calibration of the aluminum-in-hornblende geobarometer with application to long valley caldera (California) volcanic rocks. Geology 17:837–841. doi:10.1130/0091-7613(1989)017<0837:ECOTAI>2.3.CO;2

Kratzmann DJ, Carey S, Scasso RA, Naranjo JA (2010) Role of cryptic amphibole crystallization in magma differentiation at Hudson volcano, Southern Volcanic Zone, Chile. Contrib Miner Petrol 159:237–264. doi:10.1007/s00410-009-0426-1

Kushiro I (1969) System Forsterite-Diopside-Silica with and without water at high-pressures. Am J Sci 267(Suppl. I):269–294

Larocque J, Canil D (2010) The role of amphibole in the evolution of arc magmas and crust: the case from the Jurassic Bonanza arc section, Vancouver Island, Canada. Contrib Miner Petrol 159:475–492. doi:10.1007/s00410-009-0436-z

Leake BE, Woolley AR, Arps CES, Birch WD, Gilbert MC, Grice JD, Hawthorne FC, Kato A, Kisch HJ, Krivovichev VG, Linthout K, Laird J, Mandarino JA, Maresch WV, Nickel EH, Rock NMS, Schumacher JC, Smith DC, Stephenson NCN, Ungaretti L, Whittaker EJW, Guo YZ (1997) Nomenclature of amphiboles: report of the subcommittee on amphiboles of the international mineralogical association, commission on new minerals and mineral names. Am Mineral 82(9–10):1019–1037

Medard E, Grove TL (2008) The effect of H_2O on the olivine liquidus of basaltic melts: experiments and thermodynamic models. Contrib Miner Petrol 155(4):417–432. doi:10.1007/s00410-007-0250-4

Moore G, Carmichael ISE (1998) The hydrous phase equilibria (to 3 kbar) of an andesite and basaltic andesite from western Mexico: constraints on water content and conditions of phenocryst growth. Contrib Miner Petrol 130:304–319. doi:10.1007/s004100050367

Müntener O, Kelemen P, Grove T (2001) The role of H_2O during crystallization of primitive arc magmas under uppermost mantle conditions and genesis of igneous pyroxenites: an experimental study. Contrib Miner Petrol 141:643–658. doi:10.1007/s004100100266

Mysen BO (2007) The solution behavior of h2o in peralkaline aluminosilicate melts at high pressure with implications for properties of hydrous melts. Geochim Cosmochim Acta 71:1820–1834. doi:10.1016/j.gca.2007.01.007

Newman S, Lowenstern JB (2002) VOLATILECALC: a silicate melt-H2O-CO2 solution model written in Visual Basic for excel. Comput Geosci 28(5):597–604

Panjasawatwong Y, Danyushevsky LV, Crawford AJ, Harris KL (1995) An experimental study of the effects of melt composition on plagioclase—melt equilibria at 5 and 10 kbar: implications for the origin of magmatic high-an plagioclase. Contrib Miner Petrol 118:420–432. doi:10.1007/s004100050024

Pichavant M, MacDonald R (2007) Crystallization of primitive basaltic magmas at crustal pressures and genesis of the calc-alkaline igneous suite: experimental evidence from St Vincent, Lesser Antilles arc. Contrib Miner Petrol 154:535–558. doi:10.1007/s00410-007-0208-6

Pownceby MI, O'Neill HSC (1994) Thermodynamic data from redox reactions at high temperatures. IV. Calibration of the Re-ReO_2 oxygen buffer from EMF and NiO+Ni-Pd redox sensor measurements. Contrib Miner Petrol 118:130–137. doi:10.1007/BF01052864

Prouteau G, Scaillet B (2003) Experimental constraints on the origin of the 1991 pinatubo dacite. J Petrol 44:2203–2241. doi:10.1093/petrology/egg075

Ridolfi F, Renzulli A, Puerini M (2010) Stability and chemical equilibrium of amphibole in calc-alkaline magmas: an overview, new thermobarometric formulations and application to subduction-related volcanoes. Contrib Miner Petrol 160:45–66. doi:10.1007/s00410-009-0465-7

Romick JD, Kay SM, Kay RW (1992) The influence of amphibole fractionation on the evolution of calc-alkaline andesite and dacite tephra from the central Aleutians, Alaska. Contrib Miner Petrol 112:101–118. doi:10.1007/BF00310958

Ruscitto DM, Wallace PJ, Kent AJR (2011) Revisiting the compositions and volatile contents of olivine-hosted melt inclusions from the Mount Shasta region: implications for the formation of high-Mg andesites. Contrib Miner Petrol 162:109–132. doi:10.1007/s00410-010-0587-y

Rutherford MJ, Devine JD (1988) The May 18, 1980, eruption of Mount St. Helens 3. Stability and chemistry of amphibole in the magma chamber. J Geophys Res 93:11,949–11,959. doi:10.1029/JB093iB10p11949

Schmidt MW (1992) Amphibole composition in tonalite as a function of pressure: an experimental calibration of the Al-in-hornblende barometer. Contrib Miner Petrol 110:304–310. doi:10.1007/BF00310745

Schuessler JA, Botcharnikov RE, Behrens H, Misiti V, Freda C (2008) Oxidation state of iron in hydrous phono-tephritic melts. Am Mineral 93:1493–1504. doi:10.2138/am.2008.2795

Sherrod DR, Scott WE, Stauffer PH (eds) (2008) A volcano rekindled: the renewed eruption of Mount St. Helens, 2004–2006. USGS professional paper 1750

Sisson TW, Grove TL (1993) Experimental investigations of the role of H_2O in calc-alkaline differentiation and subduction zone magmatism. Contrib Miner Petrol 113:143–166. doi:10.1007/BF00283225

Sisson TW, Layne GD (1993) H_2O in basalt and basaltic andesite glass inclusions from 4 subduction-related volcanoes. Earth Planet Sci Lett 117(3–4):619–635

Tiepolo M, Tribuzio R, Langone A (2011) High-Mg andesite petrogenesis by amphibole crystallization and ultramafic crust assimilation: evidence from Adamello Hornblendites (Central Alps, Italy). J Petrol 52(5):1011–1045. doi:10.1093/petrology/egr016

Tormey DR, Grove TL, Bryan WB (1987) Experimental petrology of normal MORB near the Kane Fracture Zone: 22° 25° N, mid-Atlantic ridge. Contrib Miner Petrol 96:121–139. doi:10.1007/BF00375227

Ulmer, GC (eds) (1971) Research techniques for high pressure and high temperature. Springer, New York

Zucca JJ, Fuis GS, Milkereit B, Mooney WD, Catchings RD (1986) Crustal structure of northeastern California. J Geophys Res 91:7359–7382. doi:10.1029/JB091iB07p07359